Insights into the assembly and activation of the microtubule nucleator γ-TuRC

https://doi.org/10.1038/s41586-019-1896-6

Received: 20 August 2019

Accepted: 10 December 2019

Published online: 19 December 2019

Peng Liu[1,6], Erik Zupa[1,6], Annett Neuner[1], Anna Böhler[1], Justus Loerke[2], Dirk Flemming[3], Thomas Ruppert[1], Till Rudack[4], Christoph Peter[5], Christian Spahn[2], Oliver J. Gruss[5], Stefan Pfeffer[1]* & Elmar Schiebel[1]*

Microtubules are dynamic polymers of α- and β-tubulin and have crucial roles in cell signalling, cell migration, intracellular transport and chromosome segregation[1]. They assemble de novo from αβ-tubulin dimers in an essential process termed microtubule nucleation. Complexes that contain the protein γ-tubulin serve as structural templates for the microtubule nucleation reaction[2]. In vertebrates, microtubules are nucleated by the 2.2-megadalton γ-tubulin ring complex (γ-TuRC), which comprises γ-tubulin, five related γ-tubulin complex proteins (GCP2–GCP6) and additional factors[3]. GCP6 is unique among the GCP proteins because it carries an extended insertion domain of unknown function. Our understanding of microtubule formation in cells and tissues is limited by a lack of high-resolution structural information on the γ-TuRC. Here we present the cryo-electron microscopy structure of γ-TuRC from *Xenopus laevis* at 4.8 Å global resolution, and identify a 14-spoked arrangement of GCP proteins and γ-tubulins in a partially flexible open left-handed spiral with a uniform sequence of GCP variants. By forming specific interactions with other GCP proteins, the GCP6-specific insertion domain acts as a scaffold for the assembly of the γ-TuRC. Unexpectedly, we identify actin as a bona fide structural component of the γ-TuRC with functional relevance in microtubule nucleation. The spiral geometry of γ-TuRC is suboptimal for microtubule nucleation and a controlled conformational rearrangement of the γ-TuRC is required for its activation. Collectively, our cryo-electron microscopy reconstructions provide detailed insights into the molecular organization, assembly and activation mechanism of vertebrate γ-TuRC, and will serve as a framework for the mechanistic understanding of fundamental biological processes associated with microtubule nucleation, such as meiotic and mitotic spindle formation and centriole biogenesis[4].

To understand the structural basis of microtubule (MT) nucleation in vertebrates, we purified γ-TuRCs from *X. laevis* meiotic egg extract by affinity chromatography, and confirmed the integrity of the complexes by MT nucleation analysis, immunoblotting, sucrose gradient density sedimentation and negative-stain electron microscopy (Extended Data Fig. 1). To gain insights into the relative abundance of GCP variants in the complex, we analysed the purified γ-TuRC by label-free quantification (LFQ) mass spectrometry and determined the stoichiometry of the components normalized to a 14-spoked γ-TuRC. The purified γ-TuRC contains five copies of GCP2, five copies of GCP3, two or three copies of GCP4 and one copy of GCP5 and GCP6, resulting in a 5:5:2/3:1:1 stoichiometry (Figs. 1a, 2a).

Molecular architecture of the γ-TuRC

Using cryo-electron microscopy (cryo-EM) single-particle analysis, we obtained reconstructions of the purified γ-TuRC (Extended Data Fig. 2a–e). Local resolution assessment for initial reconstructions indicated conformational flexibility (Extended Data Fig. 2f), which we compensated for computationally by splitting the γ-TuRC into segments that were refined independently (Extended Data Fig. 2e). This approach resulted in a final reconstruction at 4.8 Å global resolution, ranging from 4.5 Å to 6 Å locally (Extended Data Fig. 2g, h). The reconstruction (Fig. 1a) indicates that the γ-TuRC consists of 14 structurally similar spokes arranged in an open left-handed spiral with a diameter of approximately 32 nm and a height of around 25 nm. Each spoke consists of one GCP and one γ-tubulin bound to the conserved GCP GRIP2 domain (Fig. 1b). Resolved features distinguish the structurally closely related GCPs in the different positions and indicate that the GCP variants assemble in a defined order. Notably, the N-terminal extensions present in all GCPs except GCP4 (Extended Data Fig. 1a) were mostly not resolved, which suggests a high degree of conformational flexibility for these regions.

[1]Zentrum für Molekulare Biologie, Universität Heidelberg, DKFZ-ZMBH Allianz, Heidelberg, Germany. [2]Charite - Universitaetsmedizin Berlin, Institute for Medical Physics and Biophysics, Berlin, Germany. [3]Heidelberg University Biochemistry Center, Heidelberg, Germany. [4]Department of Biophysics, Ruhr-University Bochum, Bochum, Germany. [5]Institut für Genetik Universität Bonn, Bonn, Germany. [6]These authors contributed equally: Peng Liu, Erik Zupa. *e-mail: s.pfeffer@zmbh.uni-heidelberg.de; e.schiebel@zmbh.uni-heidelberg.de

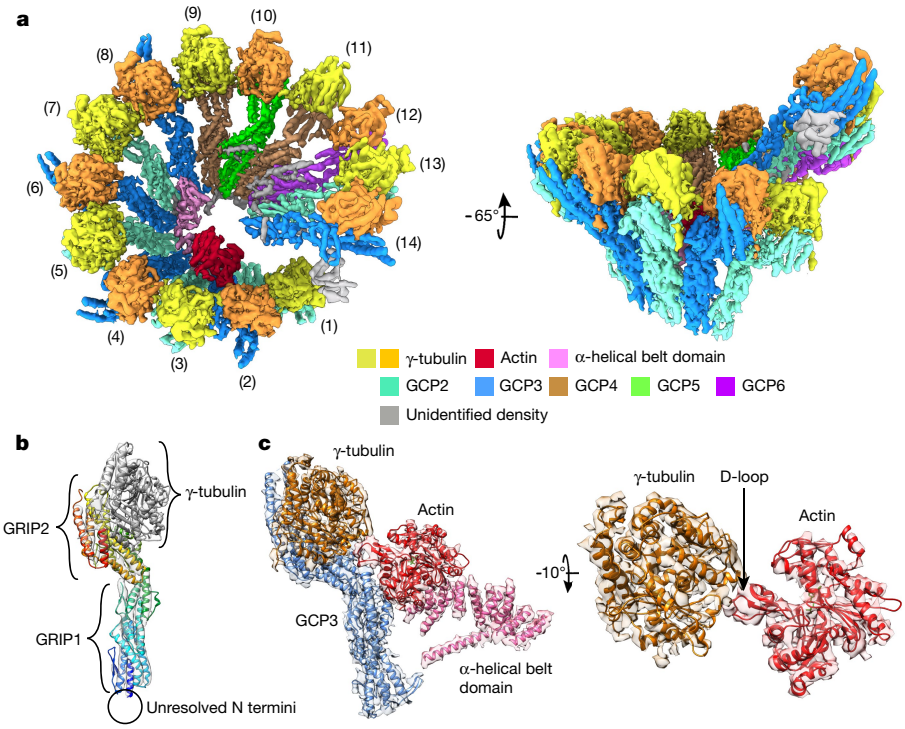

Fig. 1 | Cryo-EM structure of the *X. laevis* γ-TuRC. a, Reconstruction of the γ-TuRC, filtered according to local resolution. For each spoke, the consecutive numbering is given. **b**, General layout of a γ-TuRC spoke. Atomic models for γ-tubulin (grey) and GCP2 (rainbow-coloured from the N (blue) to the C (red) terminus) superposed to the cryo-EM density. **c**, Detailed view on molecular components involved in binding of actin.

For an initial investigation of the γ-TuRC architecture, we structurally grouped the 14 GCP–γ-tubulin spokes by computing pairwise cross-correlation coefficients between density segments for each spoke (Fig. 2b, Extended Data Fig. 3a) and by computing the pairwise root mean square deviation (r.m.s.d.) values of atomic models for human GCP4 (Protein Data Bank (PDB) code 3RIP) and γ-tubulin (PDB code 1Z5W) docked into all 14 spokes (Fig. 2b, Extended Data Fig. 3b). To account for the different conformational states of GCPs, the GCP4 model was split into three individual segments (Methods), which were then docked independently. Both approaches clustered the spokes into 5 groups with 5:5:2:1:1 stoichiometry, namely: (i) spokes 1, 3, 5, 7 and 13; (ii) spokes 2, 4, 6, 8 and 14; (iii) spokes 9 and 11; (iv) spoke 10; and (v) spoke 12. In combination with LFQ mass spectrometry (Fig. 2a), this indicates that the most abundant GCP groups (i) and (ii) correspond to GCP2 and GCP3. Most prominently, GCPs in these two groups were structurally distinguished by the length of two α-helices in the GRIP2 domain (Fig. 2c, Extended Data Fig. 3c). These two helices were predicted to be considerably longer in GCP3 than in all other GCP variants (Extended Data Fig. 4a), which allows unambiguous assignment of group (ii) to GCP3 and conversely indicates that GCPs in group (i) correspond to GCP2. This could be confirmed by a GCP2-specific extended loop (Extended Data Fig. 4b) between two GRIP2 β-strands visible exclusively in the density for group (i) spokes (Fig. 2c, Extended Data Fig. 3c). Structural clustering in conjunction with LFQ mass spectrometry also suggested that group (iii) with spokes at positions 9 and 11 corresponded to GCP4. GCP4 is the only GCP variant without an N-terminal extension (Extended Data Fig. 1a), and only group (iii) spokes had no continuous density extending from the very N-terminal helix (Fig. 2c, Extended Data Fig. 3d). Although the two remaining spokes (spokes

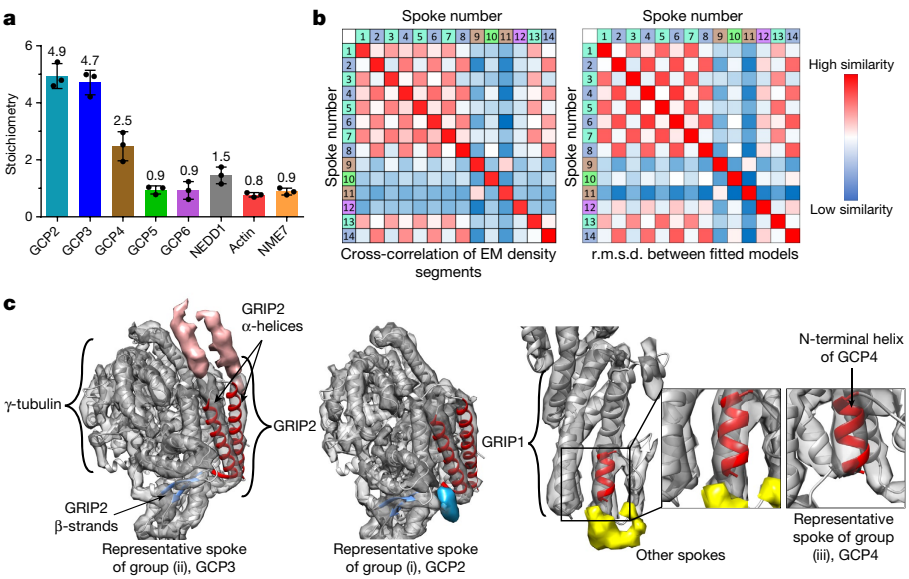

Fig. 2 | Structural clustering of γ-TuRC spokes. a, Relative abundance of γ-TuRC components as determined by LFQ mass spectrometry. Total number of GCP proteins is normalized to 14, and the abundance of each protein is calculated accordingly. $n = 3$ biologically independent experiments; data are mean ± s.d. **b**, Left, pairwise cross-correlation coefficients between density segments. Extended Data Figure 3a provides correlation values. Right, pairwise r.m.s.d. values between Cα atoms of rigid-body-fitted atomic models (Methods) representing the individual spokes. Extended Data Figure 3b provides r.m.s.d. values. **c**, Cluster-specific structural features. Left, GCP3-specific extended C-terminal α-helices (red model and density) are unique for group (ii), and a GCP2-specific extended loop between the GRIP2 β-strands (blue model and density) is present only in group (i). Right, only group (iii) spokes are devoid of continuous density (yellow) connecting to the N-terminal helix (red) of the fitted GCP4 model. See Extended Data Fig. 3c, d for features for all spokes.

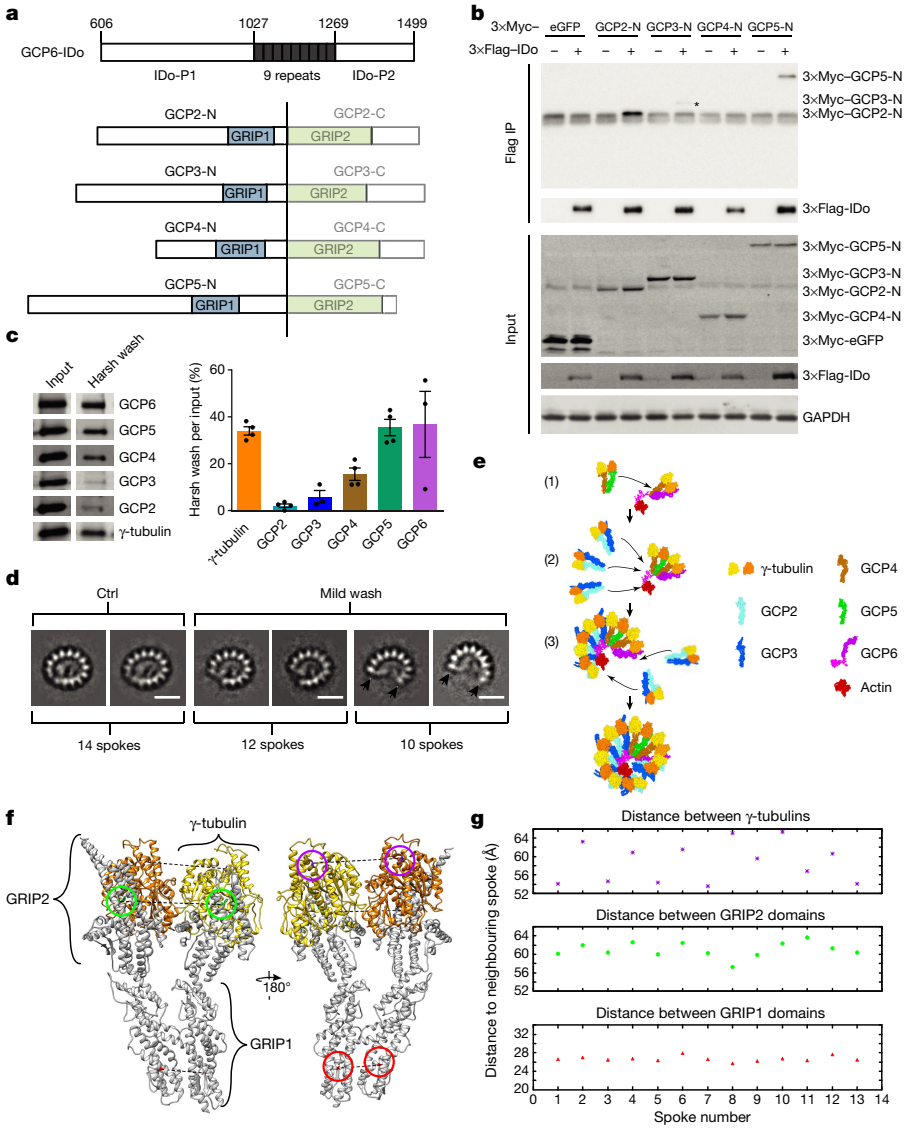

Fig. 3 | The GCP6 insertion domain assists in a stepwise assembly process of the γ-TuRC. a, Protein constructs for immunoprecipitation. IDo, insertion domain. **b**, Co-immunoprecipitation (IP) of 3×Flag–GCP6 insertion domain with the 3×Myc-tagged N terminus of GCP proteins. 3×Myc–eGFP was used as a negative control. The indicated antibodies were used for immunoblotting. Result is representative of three independent experiments. Asterisk denotes faint band of 3×Myc–GCP3-N. For gel source data, see Supplementary Fig. 1. **c**, After high-salt treatment (harsh wash), fragmented γ-TuRCs were eluted and analysed by immunoblotting. Input was purified γ-TuRC. For gel source data, see Supplementary Fig. 1. Right, quantification of immunoblots; $n = 3$ (GCP3), 4 (γ-tubulin), 4 (GCP2), 4 (GCP4), 4 (GCP5) and 3 (GCP6) biologically independent experiments; data are mean ± s.e.m. **d**, After mild salt treatment, fragmented γ-TuRCs were eluted and analysed by negative-stain electron microscopy. Representative 2D classes from three biologically independent experiments with similar results are shown. Black arrows point to the open ends. Scale bars, 20 nm. Ctrl, control. **e**, Potential stepwise assembly of the γ-TuRC. (1) Stable GCP4–GCP5 and GCP4–GCP6 heterodimers form the GCP4–GCP5–GCP4–GCP6 core. (2) Three GCP2–GCP3 heterodimers are recruited by interactions of N-GCP2 with the GCP6 insertion domain. (3) Two GCP2–GCP3 heterodimers bind to both ends of the 10-spoke intermediate. **f**, Three points were defined along the entire spoke based on the Cα atoms of conserved amino acid residues (Ala in GRIP1 (red); Phe in GRIP2 (green); and Asn in γ-tubulin (magenta)). **g**, Distances between the points were computed for each spoke and its neighbour along the helical sequence. Colours are as in **f**.

10 and 12) lacked distinguishing structural features of the GCP core segments, LFQ mass spectrometry (Fig. 2a) indicated that they correspond to the single copies of GCP5 and GCP6. Notably, we could not trace the GCP5 and GCP6 insertion domains (Extended Data Fig. 1a) in the cryo-EM reconstruction, which suggests that at least the segments directly associated with the GCP core fold are not well-ordered.

We next generated homology models for the core segments of *X. laevis* GCP2–GCP6 and *X. laevis* γ-tubulin using X-ray structures of human GCP4[5] and γ-tubulin[6], respectively and refined them against the cryo-EM density (Methods). The resulting atomic model had good statistics (Extended Data Table 1) and was validated against our cryo-EM density (Extended Data Fig. 2h). Consistent with the determined local resolution (Extended Data Fig. 2g), bulky amino acid side chains were resolved in many areas of the density and corresponded with the refined homology models (Extended Data Fig. 5, Methods). GCP-variant-specific bulky amino acid side chains confirmed our previous assignment of GCP identities for GCP2–GCP4 and also allowed identification of GCP5 (spoke 10) and GCP6 (spoke 12) in the cryo-EM density, thus establishing an atomic model for the structural core of the vertebrate γ-TuRC with a uniform sequence of GCPs: GCP(2–3)$_4$–GCP4–GCP5–GCP4–GCP6–(GCP2–3) (Fig. 1a). This order was unexpected because GCP4, GCP5 and GCP6 had previously been proposed to cap the γ-TuRC spiral[3,7].

Actin is an integral part of the γ-TuRC

Several density segments remained unexplained (Fig. 1a), and the most prominent was a belt of density lining the interior of the γ-TuRC that was already visible in the negatively stained γ-TuRC particles (Extended Data Fig. 1h, i). For assignment of these density segments, we pursued an unbiased structure-guided approach (Methods), which we verified by localizing γ-tubulin and GCP4 in the γ-TuRC as positive controls (Extended Data Fig. 6a) and ovalbumin as a negative control (Extended Data Fig. 6b). We were unable to localize established γ-TuRC components, including NEDD1 and NME7 that were identified by LFQ mass spectrometry (Fig. 2a), and MOZART1 (Extended Data Fig. 6c), which suggests that they are not covered in our cryo-EM reconstruction and probably associate with the unresolved GCP N termini. Many other proteins found to be abundant in the purified γ-TuRC could also not be localized (Methods). Unexpectedly, actin—also identified as a putative γ-TuRC component (Fig. 2a)—produced an unambiguous fit in a globular domain of the belt density (Fig. 1c, Extended Data Fig. 6d), where it bridges an α-helical belt domain with the γ-tubulin of spoke 2 (Fig. 1c). Actin binds to γ-tubulin via its D-loop—a canonical interaction also involved in the formation of actin filaments and DNaseI binding[8]. We confirmed the presence of actin by immunoblotting (Extended Data Fig. 6e) and showed that it colocalized with GCP6 by immunofluorescence microscopy (Extended Data Fig. 6f, g). Centrosomes have

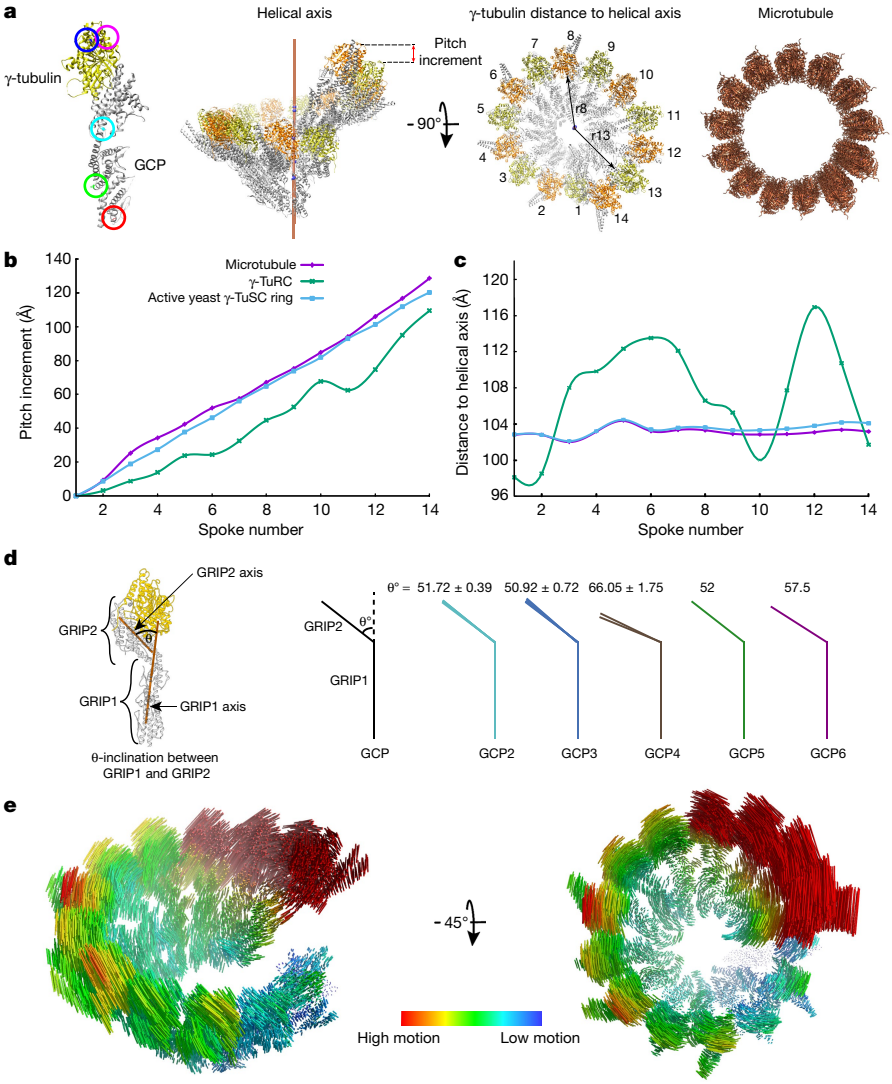

Fig. 4 | Geometrical and conformational analysis of the γ-TuRC. a, Residues distributed along each spoke (coloured circles) were used to define centroids of the approximate helical axis (brown). An MT cross-section is shown for comparison. **b**, Spokewise elevation along the helical axis (incremental pitch) for the γ-TuRC, the closed γ-TuSC spiral (PDB code 5FLZ) and a 13-spoked MT (PDB code 6EW0). **c**, Distance of γ-tubulins from the helical axis, plotted for the same complexes as in **b**. **d**, Inclinations between GRIP1 and GRIP2 axes, as defined in the atomic model. Average inclinations for the different GCP variants; data are mean ± s.e.m. $n = 5$ (GCP2), 5 (GCP3), 2 (GCP4), 1 (GCP5) and 1 (GCP6) according to the stoichiometry in the γ-TuRC. **e**, Conformational changes required for activation of the γ-TuRC visualized via vectors linking residues in both conformations. Vector length is colour-coded. See Supplementary Videos 1 and 2 for visualization of the conformational change.

previously been proposed to nucleate not only MTs but also actin filaments[9] and we therefore tested whether γ-TuRC-associated actin could be involved. Although the ARP2/3–VCA complex used as control showed robust actin filament nucleation activity in vitro, the purified γ-TuRC was inactive (Extended Data Fig. 6h). We next used an inhibition experiment to test whether γ-TuRC-associated actin could have a role in MT nucleation. The actin-binding protein DNaseI binds the actin D-loop with high affinity, and thus competes with actin binding to the γ-tubulin of spoke 2[8]. DNaseI treatment of purified γ-TuRC significantly inhibited their MT nucleation activity in vitro, and pre-incubation of DNaseI with actin abolished this effect (Extended Data Fig. 6i, j). Thus, actin is a bona fide structural component of the γ-TuRC, and has functional relevance in MT nucleation.

GCP6 assists in assembly of the γ-TuRC

Candidates for representing the remaining mostly α-helical belt density are the insertion domains of GCP5 and GCP6. The GCP5 insertion domain is comparably short (120 residues) and predicted to be mostly unordered (Extended Data Fig. 4c). By contrast, the 750-residue-long GCP6 insertion domain contains a segment of 249 residues predicted to be highly α-helical (approximately 70%) (Extended Data Fig. 4d), which we confirmed by circular dichroism spectroscopy (Extended Data Fig. 4e). Furthermore, the length of this GCP6 segment is in good agreement with the size of the α-helical belt domain (Methods), rendering the GCP6 insertion domain a genuine candidate for representing this part of the cryo-EM density.

Our cryo-EM density suggests a direct interaction between the α-helical belt domain and the N-terminal region of various GCP proteins. Following this observation, we analysed whether the human GCP6 insertion domain (residues 606–1499) (Fig. 3a) has the ability to interact with N-terminal domains of human GCP proteins. Indeed, the N-terminal domains of GCP2 and GCP5 (GCP2-N and GCP5-N, respectively) were robustly co-immunoprecipitated with the GCP6 insertion domain (Fig. 3b), whereas GCP3-N showed only weak binding (Fig. 3b, asterisk). Enhanced green fluorescent protein (eGFP) that was

used as control and GCP4-N were not detected. To narrow down which regions of the GCP6 insertion domain interact with GCP-N termini, we divided the human GCP6 insertion domain into three subdomains (Fig. 3a). GCP2-N and GCP5-N interacted specifically with the mostly conserved α-helical GCP6(606–1026) fragment, denoted part 1 of the GCP6 insertion domain, which consequently could mediate specific recruitment of GCP2 and GCP5 to the γ-TuRC (Extended Data Figs. 7a, 8). Mutations that disrupt the α-helical structure (Extended Data Fig. 8) strongly reduced binding to GCP2-N and GCP5-N (Extended Data Fig. 7b), which validates the role of the GCP6 insertion domain for GCP recruitment. In contrast to the α-helical region, the nine repeats in the GCP6 insertion domain did not interact with GCP2 and GCP5 (Extended Data Fig. 7a). Differential extraction of GCP variants from the purified γ-TuRC by salt treatment suggests a stable core of GCP4, GCP5 and GCP6 that is resistant to harsh salt treatment (Fig. 3c). Mild salt treatment depleted γ-TuRC of peripheral GCP subunits (most likely GCP2–GCP3 complexes), as indicated by negative-stain 2D classes (Fig. 3d). These data suggest a stepwise assembly mechanism in which the GCP6 insertion domain mediates specific recruitment of one pre-assembled GCP4–GCP5 dimer[10] to a GCP4–GCP6 core[11], before the binding of preformed GCP2–GCP3 complexes (Fig. 3e). The presence of preformed GCP2–GCP3 complexes is not only supported by their concomitant loss after a salt wash always resulting in even-spoked γ-TuRCs (Fig. 3d), but also by the observation of a pairwise pattern in the distances of GCP and γ-tubulin molecules, indicating tighter interaction within the GCP2–GCP3 dimers compared with interdimer interactions (Fig. 3f, g).

Conformational activation of the γ-TuRC

In vertebrates, the γ-TuRC is assembled in a state with only basal MT nucleation activity and activators are required to stimulate MT nucleation[12,13]. To gain insights into the structural basis of γ-TuRC activation, we explored whether the geometry of the γ-TuRC in our cryo-EM reconstruction would be compatible with templating MT nucleation. We approximated the γ-TuRC helical axis (Fig. 4a) and, for each spoke, determined the incremental γ-tubulin elevation along the axis (Fig. 4b) and the helix radius (Fig. 4c). We observed no strict helical symmetry for both parameters, which indicates that the purified γ-TuRC was geometrically incompatible with being a structural template for a 13-spoked MT (Fig. 4b, c). To understand the structural basis for the observed deviations in helical symmetry, we analysed the intrinsic conformational arrangement of GRIP1 and GRIP2 domains for each individual spoke. The domain arrangement was similar for all copies of GCP2, GCP3 and GCP5, but differed for GCP4 and GCP6 (Fig. 4d). Here, the GRIP domains were arranged in a more-stretched conformation, resulting in position-specific displacement of the γ-tubulins that could contribute to the observed distortion of helical symmetry. We extrapolated the structure of an MT-nucleation-competent γ-TuRC based on the previously described *Saccharomyces cerevisiae* γ-TuSC spiral[14] known to have high MT nucleation activity, and visualized the required global conformational rearrangement, mostly representing a contraction of the γ-TuRC spiral that is accompanied by repositioning of γ-tubulins to achieve a uniform spacing that reflects MT symmetry (Fig. 4e, Supplementary Videos 1, 2). Such structural rearrangements could occur spontaneously during MT nucleation, explaining the basal nucleation activity of purified γ-TuRC in vitro (Extended Data Fig. 1c), or they could be induced by activators of MT nucleation such as CEP215[12]. To test the latter hypothesis, we added the purified CEP215 N terminus (CEP215-N) including the activating CM1 motif in large excess to purified γ-TuRC, and analysed the structural and functional properties of the complexes using negative-stain electron microscopy and in vitro MT nucleation assays (Extended Data Fig. 9a, b). Although CEP215-N bound to γ-TuRC in vitro (Extended Data Fig. 9c), we did not observe structural changes or a strong increase in MT nucleation activity, which suggests the requirement of other factors that potentially act together with CEP215-N. Consistently, the addition of recombinant CEP215-N to egg extract stimulated MT nucleation only in combination with Ran(Q69L) (loaded with GTP)—a GTP-hydrolysis-defective mutant of the GTPase Ran (Extended Data Fig. 9d). Notably, the N terminus of the CEP215(F75A) mutant[12] that was less efficient in γ-TuRC binding (Extended Data Fig. 9c) could not stimulate MT nucleation activity in egg extract (Extended Data Fig. 9d).

Collectively, these biochemical and structural data fundamentally deepen our understanding of MT nucleation by providing detailed insights into the molecular organization, assembly and activation mechanism of vertebrate γ-TuRC. Our study provides a rationale for the evolutionary acquisition of the GCP4–GCP6 variants in vertebrates. In contrast to budding yeast, in which the MT nucleating template is assembled only at the yeast centrosome for local MT nucleation[14], our data suggest that the acquisition of GCP4 and GCP6—both contributing to the asymmetry of γ-TuRC—enables context-independent pre-assembly of inactive γ-TuRC that can be efficiently activated via a conformational change. This allows much faster and more dynamic regulation of MT nucleation within the assembling mitotic spindle, in which hundreds to thousands of MTs have to be nucleated within minutes[15].

Online content

Any methods, additional references, Nature Research reporting summaries, source data, extended data, supplementary information, acknowledgements, peer review information; details of author contributions and competing interests; and statements of data and code availability are available at https://doi.org/10.1038/s41586-019-1896-6.

1. Borisy, G. et al. Microtubules: 50 years on from the discovery of tubulin. *Nat. Rev. Mol. Cell Biol.* **17**, 322–328 (2016).
2. Zheng, Y., Wong, M. L., Alberts, B. & Mitchison, T. Nucleation of microtubule assembly by a γ-tubulin-containing ring complex. *Nature* **378**, 578–583 (1995).
3. Kollman, J. M., Merdes, A., Mourey, L. & Agard, D. A. Microtubule nucleation by γ-tubulin complexes. *Nat. Rev. Mol. Cell Biol.* **12**, 709–721 (2011).
4. Schmidt-Cernohorska, M. et al. Flagellar microtubule doublet assembly *in vitro* reveals a regulatory role of tubulin C-terminal tails. *Science* **363**, 285–288 (2019).
5. Guillet, V. et al. Crystal structure of γ-tubulin complex protein GCP4 provides insight into microtubule nucleation. *Nat. Struct. Mol. Biol.* **18**, 915–919 (2011).
6. Aldaz, H., Rice, L. M., Stearns, T. & Agard, D. A. Insights into microtubule nucleation from the crystal structure of human γ-tubulin. *Nature* **435**, 523–527 (2005).
7. Moritz, M., Braunfeld, M. B., Guénebaut, V., Heuser, J. & Agard, D. A. Structure of the γ-tubulin ring complex: a template for microtubule nucleation. *Nat. Cell Biol.* **2**, 365–370 (2000).
8. Kabsch, W., Mannherz, H. G., Suck, D., Pai, E. F. & Holmes, K. C. Atomic structure of the actin:DNase I complex. *Nature* **347**, 37–44 (1990).
9. Farina, F. et al. The centrosome is an actin-organizing centre. *Nat. Cell Biol.* **18**, 65–75 (2016).
10. Farache, D. et al. Functional analysis of γ-tubulin complex proteins indicates specific lateral association via their N-terminal domains. *J. Biol. Chem.* **291**, 23112–23125 (2016).
11. Anders, A., Lourenço, P. C. & Sawin, K. E. Noncore components of the fission yeast γ-tubulin complex. *Mol. Biol. Cell* **17**, 5075–5093 (2006).
12. Choi, Y. K., Liu, P., Sze, S. K., Dai, C. & Qi, R. Z. CDK5RAP2 stimulates microtubule nucleation by the γ-tubulin ring complex. *J. Cell Biol.* **191**, 1089–1095 (2010).
13. Scrofani, J., Sardon, T., Meunier, S. & Vernos, I. Microtubule nucleation in mitosis by a RanGTP-dependent protein complex. *Curr. Biol.* **25**, 131–140 (2015).
14. Kollman, J. M., Polka, J. K., Zelter, A., Davis, T. N. & Agard, D. A. Microtubule nucleating γ-TuSC assembles structures with 13-fold microtubule-like symmetry. *Nature* **466**, 879–882 (2010).
15. Petry, S. & Vale, R. D. Microtubule nucleation at the centrosome and beyond. *Nat. Cell Biol.* **17**, 1089–1093 (2015).

Methods

Data reporting

No statistical methods were used to predetermine sample size. The experiments were not randomized and investigators were not blinded to allocation during experiments and outcome assessment.

Plasmid construction

PCR amplifications were performed with Q5 High Fidelity DNA Polymerase (NEB). Fragments were inserted into the backbones with NEBuilder HiFi DNA Assembly Cloning Kit (NEB). To generate 3×Flag-tagged GCP6 constructs, corresponding fragments for the GCP6 insertion domain (residues 606–1499, denoted GCP6-IDo), the 4P mutant of the GCP6 insertion domain (denoted GCP6-IDo^{4P}), the GCP6 insertion domain part 1 (residues 606–1026, denoted IDo-P1), the 4P mutant of the GCP6 insertion domain part 1 (denoted IDo-P1^{4P}), the GCP6 insertion domain 9 repeats (residues 1027–1268, denoted IDo-9 repeats) and the GCP6 insertion domain part 2 (residues 1269–1499, denoted IDo-P2) were amplified and inserted into BamHI-digested pRetroX-TRE3G vector and sub-cloned into pCMV-3Tag-1A vector via BamHI. To generate 3×Myc-tagged GCP6 constructs, eGFP, GCP2-N (1–1485 bp), GCP3-N (1–1620 bp), GCP4-N (1–1008 bp) and GCP5-N (1–2142 bp) were amplified and inserted into the BamHI site of pCMV-3Tag-2B. An additional base pair 'A' was introduced upstream to avoid frameshift and the BamHI site was regenerated downstream. The coding sequence for residues 546–794 of *X. laevis* GCP6 (xGCP6(546–794)) was amplified and inserted into a BamHI-digested pGEX-6P-1 vector to generate pGEX-6P1-xGCP6(546–794). Subsequently, the plasmid was digested with EcoRI/NotI and a StrepII tag was introduced after the coding sequence of xGCP6(546–794).

Antibodies

Anti-γ-tubulin rabbit polyclonal antibody, which was used for γ-TuRC purification and the CEP215-N pull-down assay, was generated against the C-terminal peptide[2]. Anti-γ-tubulin mouse monoclonal antibody (GTU-88), which was used for immunoblotting, was from Sigma-Aldrich. Rabbit anti-GCP2 polyclonal antibody was from Thermo Fisher Scientific. Rabbit anti-GCP3 polyclonal antibody and rabbit anti-GCP6 polyclonal antibodies were from Y. Zheng. Guinea-pig anti-GCP6 polyclonal antibody for immunofluorescence was generated as previously described[16]. Anti-β-actin mouse monoclonal antibody (AC-74) used in immunofluorescence and anti-actin rabbit polyclonal antibody (A2066) used in immunoblotting were from Sigma-Aldrich. Anti-GCP4 rabbit polyclonal antibodies were raised against full-length purified GCP4. Anti-GCP5 mouse monoclonal antibody (E-1) was from Santa Cruz Biotechnology. Mouse anti-Flag monoclonal antibody (9A3) and rabbit anti-GAPDH polyclonal antibody (14C10) were from Cell Signaling Technology. Mouse monoclonal anti-Myc antibody (clone 9E10) was from Sigma-Aldrich. Secondary antibodies were: donkey anti-mouse Alexa Fluor 488-conjugated antibody and goat anti-guinea pig Alexa Fluor 555-conjugated antibody (Thermo Fisher Scientific); peroxidase-conjugated goat anti-mouse antibody (Jackson ImmunoResearch Laboratories); donkey anti-mouse DyLight 680 and 800-conjugated antibodies (Thermo Fisher Scientific); anti-rabbit DyLight 680-conjugated antibody (Cell Signaling Technology); IRDye 800CW Donkey anti-Rabbit IgG (LI-COR Biosciences).

γ-TuRC purification

CSF-arrested *X. laevis* egg extracts were prepared as previously described[17] and stored at −80 °C. To purify the γ-TuRCs, an adequate amount of egg extracts was defrosted and incubated with γ-tubulin antibody-crosslinked Dynabeads Protein A for 30 min at room temperature and subsequently washed with: (1) 3 times with CSF-XB buffer (5 mM EGTA, 10 mM HEPES pH7.7, 2 mM $MgCl_2$, 50 mM sucrose, 100 mM KCl, 0.1 mM $CaCl_2$); (2) 3 times with CSF-XB buffer supplemented with 250 mM KCl and 0.3% Triton X-100; and (3) twice with HB100 buffer (50 mM Na-HEPES pH 8.0, 1mM EGTA, 1 mM $MgCl_2$, 100 mM NaCl) containing 0.1 mM GTP. Elution was performed overnight at 4 °C with gentle rotation in HB100 buffer containing 0.1 mg ml^{-1} γ-tubulin antigenic C-terminal peptide[2], 1 mM GTP and 0.02% Tween20. The concentration of the purified γ-TuRCs was determined as 5 nM by immunoblotting comparing to purified human γ-tubulin.

γ-TuRC salt treatments

Both mild and harsh washing were performed with the same protocol as γ-TuRC purification except washing step (2). For the mild washing, washing step (2) was carried out with CSF-XB buffer supplemented with 500 mM KCl and 0.3% Triton X-100 (3 times). For harsh washing, washing step (2) was carried out sequentially with CSF-XB buffer containing 0.3% Triton X-100 and 4 different concentrations of additional KCl: 250 mM (4×), 500 mM (1×), 750 (1×) and 1 M (1×). The beads were washed with each buffer for 15–20 min (at 4 °C with gentle rotation) and the proteins were eluted as described in the γ-TuRC purification protocol. The band intensity was quantified with the software Image Studio Lite (v.5.2.5, LI-COR Biosciences) using the Analysis function.

In-gel tryptic digestion, LC–MS/MS analysis and database search

Samples were separated by SDS–PAGE (minigel, 10%; Invitrogen) for 1.0 cm. Coomassie-stained lanes were cut out with a scalpel and processed as previously described[18]. In brief, samples were reduced with dithiothreitol (DTT), alkylated with iodoacetamide and digested with trypsin. Peptides were extracted from gel pieces, concentrated in a speedVac vacuum centrifuge and dissolved with 15 µl 0.1% trifluoroacetic acid. Nanoflow LC-MS2 analysis was performed with an Ultimate 3000 liquid chromatography system coupled to an Orbitrap Elite mass spectrometer (Thermo-Fisher). Five microlitres of sample was injected to a self-packed analytical column (75 mm × 200 mm; ReproSil Pur 120 C18-AQ; Dr. Maisch) and eluted with a flow rate of 300 nl min^{-1} in an acetonitrile-gradient (3–40%). One survey scan (resolution: 60,000) was followed by 15 information-dependent product ion scans in the ion trap. The MaxQuant software (1.6.2.6a)[19] was used with default settings for database search against a *X. laevis* database downloaded from UniProt.org (Proteome ID: UP000186698 with 42.878 entries; last modified October 2018) together with the contaminants database included in the MaxQuant software. In addition, a custom-made database (Supplementary Table 2) was used containing additional database entries for γ-tubulin complex components not identical with the UniProt entries. Trypsin was specified as enzyme. Carbamidomethyl was set as fixed modification of cysteine and oxidation (methionine), deamidation (asparagines and glutamine) and N-terminal acetylation as variable modifications. A false-discovery rate of 1% was used on peptide and protein levels. To calculate iBAQ values[20], an additional MaxQuant analysis was used with iBAQ calculation enabled. An Andromeda score threshold of 40 was set for unmodified peptides to avoid false positives for quantification. For calculation of stoichiometries, the calculated iBAQ values of the database entries Q5PQ98 (γ-tubulin), O73787 (GCP3), A0A1L8H0R3 (GCP4), A0A1L8HGZ5 (GCP5), A0A1L8GZ56 (GCP6), A0A1L8GY92 (NEDD1), A0A1L8EXC8 (actin) and A0A1L8HF79 (NME7) from UniProtKB and XP_018080016.1 (GCP2) from the NCBI database were used. To account for different degrees of purity among different preparations of γ-TuRC, data were normalized to the iBAQ values of GCP2 and GCP3. Source data for LFQ mass spectrometry are included in Supplementary Table 1.

Immunoprecipitation

Mycoplasm-free HEK293T cells were bought from ATCC (American Type Culture Collection) and grown in Gibco DMEM/F-12 medium (Thermo Fisher Scientific) supplemented with 10% fetal bovine serum, 2 mM L-glutamine, 100 U ml^{-1} penicillin and 100 µg ml^{-1} streptomycin at 37 °C with 5% CO_2. Plasmids were transiently transfected at 40–50%

cell confluency in 10-cm dishes with polyethylenimine according to the standard protocol. Then, 18–36 h after transfection, cells were scraped and lysed with lysis buffer containing 10 mM Tris-HCl, pH 7.5, 150 mM NaCl, 0.5% NP40, 0.5 mM EDTA, 1 tablet per 50 ml protease inhibitor cocktail (cOmplete, EDTA-free, Roche) and 1:500 Benzonase (Merck Millipore). After pipetting 20 times and passing through a 21Gx1½ (0.8 × 40 mm) needle 20 times, the mixture was placed on ice for 10 min and clarified by spinning for 20 min, 20,000*g* at 4 °C. The supernatant was collected and incubated with 25–30 µl anti-Flag M2 affinity gel (Sigma-Aldrich, equilibrated with the lysis buffer) for 2 h at 4 °C on a rotating wheel. The beads were collected by centrifuging at 6,000*g*, 4 °C for 30 s. After washing once with lysis buffer and three times with PBS, the proteins on the beads were eluted by incubating with 2× sample buffer at 65 °C for 15 min.

Silver staining

Polyacrylamide 10–12% gels were used in this study. For silver staining, the gel was incubated for 30 min in fixing solution containing 40% methanol and 10% acetic acid. Excess acetic acid was washed away with 30% methanol followed by three washes with water. The gel was sensitized for 2 min in 0.02% freshly prepared NaS_2O_3 and then washed with water. The staining was performed with 0.2% $AgNO_3$ at 4 °C for 25 min, and residual $AgNO_3$ was washed away with water. The development was performed with 6% Na_2CO_3, 0.05% formaldehyde and 0.0004% NaS_2O_3, and the reaction was terminated with 1.4% EDTA when the staining was sufficient. Major bands from the gel in Extended Data Fig. 1d were cut out and verified by mass spectrometry.

In vitro MT nucleation assay

Unlabelled and Cy3-labelled pig brain tubulin were mixed 24:1 in 1× BRB80 buffer (80 mM PIPES/KOH pH 6.8, 1 mM $MgCl_2$ and 1 mM EGTA) with a final glycerol concentration of 12.5% (w/v). After spinning at 352,860*g*, 4 °C for 5 min with S100-AT3 rotor (Thermo Fisher Scientific), 2.5 µl supernatant and 2.5 µl γ-TuRC mixture (0.2 µl γ-TuRC, 1 mM GTP, 12.5% (w/v) glycerol in 1× BRB80 buffer) were used, incubated for 15–30 min on ice and transferred to a 37-°C water bath for 5 min for MT nucleation. The sample was immediately mixed with 50 µl 1% glutaraldehyde in 1× BRB80 buffer and incubated for 5 min at room temperature for crosslinking. Then, 1 ml cold 1× BRB80 buffer was added to stop the reaction and 50 µl of sample was mounted onto a 2 ml 10% glycerol, BRB80 cushion in a Corex 15-ml glass tube with a 12-mm coverslip supported by a glass platform at the bottom. The MTs were sedimented onto poly-lysine-coated coverslips by centrifuging with an HB4/HB6 rotor (Thermo Fisher Scientific) at 23,530*g* for 1 h at 20 °C. After fixing for 5 min in ice-cold methanol, the sample was mounted on a 2 µl drop of Citiflour AF1 (Electron Microscopy Sciences) and sealed with nail polish. For each sample, 20 random images were acquired using an Axiovert 200 M microscope (Carl Zeiss Microscopy) equipped with a Plan-Apochromat 63× NA 1.3 oil objective lens (Carl Zeiss Microscopy), and a Cascade1 K EMCCD camera (Photometrics). Imaging was operated with VisiView and the images were processed with ImageJ.

DNaseI inhibition assay

Purified γ-TuRC was incubated with a 100-fold excess of recombinant DNaseI (Sigma-Aldrich, D5319) for 3 h on ice. As a control, DNaseI and G-actin were pre-incubated in a 1:1 ratio for 1 h on ice, and the mixture was subsequently added to the purified γ-TuRC. The protocol for the in vitro MT nucleation assay was performed as described above except: after the addition of 1 ml cold 1× BRB80 buffer to stop the reaction, 3 µl of sample was squash-fixed on a slide with a 12 × 12-mm^2 coverslip. The imaging protocol was as described above and the MT number was counted manually from 20 random fields. For each sample, five random images were compiled into a stack and the maximum projection was presented in Extended Data Fig. 9b. This protocol is the same for the in vitro MT nucleation assay of γ-TuRC with CEP215-N.

Sucrose gradient

Sucrose gradients were made by a Model 106 Gradient Master (BioComp Instruments) according to standard instructions. Purified γ-TuRC was loaded onto a 2.2-ml 5–40% gradient in HB100 buffer with 0.1 mM GTP. Centrifugation was performed in PA 7/16 X 2-3/8 tubes (Beckman Coulter) in the S55-S Swinging-Bucket Rotor (Thermo Fisher Scientific) at 200,000*g* for 3 h at 4 °C. The fractions were collected from the top (160 µl per fraction). In total, 13 fractions were collected and analysed by immunoblotting. γ-TuRC was found around fractions 8–11. Thyroglobulin 19S (660 kDa) was used as a molecular mass marker.

Protein purification

For expression of the N-terminal 249 amino acids of the xGCP6-IDo, pGEX-6P1-xGCP6(546–794)-Strep II was transformed into *Escherichia coli* strain BL21-CodonPlus(DE3)-RIL competent cells. The transformed cells were cultured in 2xYT medium, and protein expression was induced with 0.2 mM isopropyl β-D-1-thiogalactopyranoside (IPTG) at an optical density of 0.5–0.8. After induction for 5 h at 25 °C, cells were collected, washed with PBS and stored at −80 °C. The pellets were resuspended in lysis buffer containing 50 mM Tris, 150 mM NaCl, 10% glycerol, pH 8, 1 mM EDTA, 1 mM DTT, 5 mM ATP, 2 mM $MgCl_2$, 0,1% Triton X-100, cOmplete EDTA-free protease inhibitor cocktail (Roche) and PMSF. Afterwards, the cells were lysed by sonification. The cell lysate was clarified by centrifuging at 45,000 rpm for 25 min with Type 50.2 Ti Rotor (Beckman Coulter). The supernatant was incubated with the pre-equilibrated Protino Glutathione Agarose 4B (MACHEREY-NAGEL), and the protein was eluted by 3C protease cleavage. The eluates were bound to StrepTactin TM Sepharose High Performace (GE Healthcare) and eluted with 2.5 mM desthiobiotin.

For purification of GST, GST–CEP215-N and GST–CEP215(F75A)-N, the protocol is as described for xGCP6(546–794) except the induction and elution steps. Protein expression was induced overnight at 18 °C, and after the purification washing steps, proteins were eluted with 30 mM reduced L-glutathione (Sigma-Aldrich) in 50 mM Tris, 150 mM NaCl, 10% glycerol, pH 8 and 1 mM EDTA. Eluted proteins were further purified using a Mono Q 5/50 GL anion exchange column (GE Healthcare) to remove the reduced L-glutathione.

Circular dichroism spectroscopy

Purified xGCP6(546–794) was dialysed against 50 mM Na_2HPO_4-NaH_2PO_4 and 150 mM NaF, pH 8 overnight and concentrated on Vivaspin 6 centrifugal concentrator (Sartorius) to a final concentration of 2.6 µM. The circular dichroism spectra were recorded on a Jasco J715 spectropolarimeter at 25 °C. A cell with a 1-mm path length was used for spectra recorded between 190 and 250 nm with sampling points every 0.2 nm. For each measurement, the spectra represented the average of five scans and circular dichroism intensities were expressed in millidegrees.

CEP215-N pull-down assay

Purified GST, GST–CEP215-N and GST–CEP215(F75A)-N were conjugated with Protino Glutathione Agarose 4B (MACHEREY-NAGEL) and pre-equilibrated with HB100 buffer with 0.1 mM GTP. Seven and a half microlitres purified γ-TuRC was incubated with the conjugated beads in a volume of 90 µl for 2 h at 4 °C. After washing 4 times with washing buffer (HB100 buffer with 0.1 mM GTP and 0.01% NP-40), bound proteins were eluted with elution buffer (HB100 buffer with 0.1 mM GTP, 0.01% NP-40 and 30 mM reduced GSH) at 4 °C for 30 min.

CEP215-N activity assay in egg extract

Freshly prepared CSF-arrested *X. laevis* egg extracts were mixed with 1 µM Cy3-labelled pig brain tubulin, 15 µM Ran(Q69L), 3 µM GST–CEP215-N or GST–CEP215(F75A)-N and incubated on ice for 1 h. After incubating in a 20-°C water bath for 15 min, 2 µl of sample was squashed on a slide with a 12 × 12-mm^2 coverslip to test for aster formation. Ten random images

were acquired for each sample using an Axiovert 200 M microscope (Carl Zeiss Microscopy) equipped with a 10× objective lens (Carl Zeiss Microscopy), and a Cascade1 K EMCCD camera (Photometrics). Imaging was operated with VisiView. The images were processed with ImageJ and the fluorescence intensity of the asters in 10 images was quantified.

Immunofluorescence microscopy

Purified γ-TuRCs from *X. laevis* were spun on 12-mm coverslips coated with poly-L-lysine (Sigma-Aldrich) at 23.530*g*, 4 °C for 30 min with an HB6 rotor (Thermo Fisher Scientific). After fixation with ice-cold methanol for 5 min at −20 °C, samples were incubated with PBS containing 10% FBS and 0.1% Triton X-100 for 30 min at room temperature and subsequently treated with 1% SDS in PBS for 5 min at room temperature. The PBS-washed coverslips were sequentially incubated at room temperature with primary antibodies for 1 h and Alexa-Fluor-conjugated secondary antibodies for 30 min. A DeltaVision RT system (Applied Precision, Olympus IX71 based) equipped with the Photometrics CoolSnap HQ camera (Roper Scientific), a 100×/1.4 NA UPlanSAPO objective (Olympus), a mercury arc light source and the softWoRx software (Applied Precision) were used for imaging. Selected channels, FITC and TRITC, with different exposure times according to the fluorescence intensity of each protein, were applied. Images were acquired by softWoRx software (Applied Precision) and analysed by Fiji. Each group included at least 15 images in each independent experiment. For quantification, one randomly selected image was used as a reference for adjusting the brightness and contrast levels to optimal values and all images were analysed using the same settings. GCP6 and actin signals from images in each experiment were counted and used for quantification.

Actin polymerization assay

Pyrene-labelled actin (Hypermol) was dissolved in general actin buffer (5 mM Tris, pH 8.0, 0.2 mM $CaCl_2$, 0.2 mM ATP and 0.5 mM DTT) to a final concentration of 2 μM. The reaction contained 20 μl pyrene-labelled actin, actin polymerization buffer (final concentration with 10 mM Tris, pH 7.5, 50 mM KCl, 2 mM $MgCl_2$ and 1 mM ATP) and either 2 μl purified γ-TuRC (final concentration 0.5 nM) or 2 μl γ-TuRC elution buffer. The controls contained pyrene-labelled actin, actin polymerization buffer, γ-TuRC elution buffer, Arp2/3 (0.5 nM final concentration, Hypermol) and VCA (15 nM, Hypermol). Fluorescence was measured at 25 °C using a plate reader every 1 min for a period of 100 min (CLARIOstar, BMG Labtech, excitation, F:360-10, emission, F: 450-10).

Negative-staining electron microscopy and image analysis

Negatively stained samples were generated as follows: 5 μl of the purified γ-TuRCs were applied on a glow-discharged copper-palladium hexagonal 400 EM mesh grid covered with an approximately 10-nm-thick continuous carbon layer. After a 30 s incubation, the sample was blotted on a Whatman filter paper 50 (1450-070) and washed with three drops of water. Samples on grids were stained with 3% uranyl acetate in water. Images were acquired on an FEI Tecnai F20 electron microscope, operated at 200 kV, equipped with a field emission gun and bottom-mounted 4 K camera. The micrographs were acquired at 50,000× magnification by the SerialEM software, resulting in 2.27 Å per pixel. For 2D classification, γ-TuRC particles were selected manually using the Boxer of EMAN2[21]. Image processing was carried out using the IMAGIC-4D package[22]. Particles were band-pass-filtered and normalized in their grey value distribution, and mass-centred. Two-dimensional alignment, classification and iterative refinement of class averages were performed as previously described[23]. Approximate number of total particles for 2D classification and averaging: Fig. 3d, ctrl, 5,400; Fig. 3d, mild wash, 3,100; both Extended Data Fig. 1h, i, 2,200. For Fig. 3d and Extended Data Fig. 1h, a 46.5-nm mask was used for averaging; for Extended Data Fig. 1i, a 14.5-nm mask was used for averaging. Particles included in the representative classes of Fig. 3d: 14 spokes, left, 115, right, 139; 12 spokes, left, 67, right, 59; 10 spokes, left, 76, right, 69.

For γ-TuRCs incubated with or without CEP215-N, the negative-staining sample preparation and imaging were done as described above. For 3D classification and 3D reconstruction of γ-TuRC with or without CEP215-N, particles were manually located on the micrographs as described above. Micrographs and particle coordinates were subsequently imported into Relion 3.0 beta and particles were subjected to 3D classification into three classes using a scaled density of the γ-TuRC cryo-EM reconstruction as initial reference. For the γ-TuRC without CEP215-N, we retained all 2,205 manually selected particles and subjected them to 3D autorefinement. For the γ-TuRC with CEP215-N, we retained 1,581 of the 2,057 manually selected particles for 3D autorefinement. To compare the overall structure and conformation of the two resulting 3D reconstructions, we superposed them according to the first four spokes using the Fit in map command in UCSF Chimera. To compare the structure of the CEP215-N–γ-TuRC density with the extrapolated structure of the active γ-TuRC, we simulated the density at 30 Å resolution from the atomic model in UCSF Chimera and superposed it to the negative stain 3D reconstruction of the CEP215-N–γ-TuRC complex as described above.

Cryo-EM sample preparation

Homemade graphene oxide holey carbon grids (Cu R2/1; 300 mesh) were glow-discharged using a Gatan Solarus 950 plasma cleaner for 20 s. Cryo-EM grids were prepared using a Thermo Fisher/FEI Vitrobot Mark IV operated at 22–25 °C and 60–70% humidity. Four microlitres of purified γ-TuRCs was applied to the EM grids within the climate chamber of the Vitrobot. After a waiting time of 30 s, grids were blotted with Whatman filter paper no. 1 for 5 or 10 s and plunge-frozen in liquid ethane bath cooled by liquid nitrogen.

Cryo-EM data acquisition

Four datasets were acquired using SerialEM[24] on a Titan Krios TEM (Thermo Fisher/FEI) operated at 300 kV and equipped with a K3 camera (Gatan) operated in dose fractionation mode. Datasets 1–3 were collected at an object pixel size of 2.1 Å per pixel with cumulative doses of 35 e Å^{-2} (70 frames), 42 e Å^{-2} (60 frames) and 51 e Å^{-2} (46 frames), respectively. Dataset 4 was collected at an object pixel size of 1.35 Å per pixel with a cumulative dose of 57 e Å^{-2} (39 frames). For each preselected hole, defocus was adjusted automatically before acquisition of two (datasets 1–3) or four (dataset 4) frame stacks per hole. Data were collected in a defocus range of −0.5 to −3.5 μm.

Data processing

All image processing steps are summarized in Extended Data Fig. 2. Unless stated otherwise, image processing was carried out in RELION 3.0-beta[25]. Datasets 1–3 were initially processed separately, but following an identical workflow, which is described below. The individual numbers of frame stacks and particles retained after each processing step, as well as resolution of intermediary cryo-EM densities is included in Extended Data Fig. 2. Frame stacks were motion-corrected with MotionCorr2[26] using 5 × 5 patches. The contrast transfer function (CTF) of the motion-corrected micrographs was estimated using gCTF[27]. In total, 3,000 particles were manually selected and used to generate a purely data-driven initial 3D density of the γ-TuRC in Relion with standard parameters. Particles were autopicked in RELION using this initial 3D density, from which reference projections were automatically generated. Localized particles were extracted at 4.2 Å pixel size in boxes of 128 × 128 pixels. Particles were subjected to two rounds of 3D classification with standard parameters to successively remove false-positive particles, broken γ-TuRCs and classes with strong orientational bias. The subset of particles retained after the second round of 3D classification were recentred, extracted at full spatial resolution in boxes of 256 × 256 pixels and subjected to 3D autorefinement using solvent-flattened Fourier shell correlation (FSC) and otherwise standard parameters. After refinement, particles were subjected to per-particle CTF refinement

(including beam tilt estimation for individual datasets) and Bayesian polishing[28] trained on 1,000 particles.

Dataset 4 was the largest, and autopicked particles were divided into four different subsets to speed up initial 3D classification steps. However, following the classification strategy described above, 3D classes of sufficient quality could only be obtained for two of the four subsets as the ratio of true- to false-positive particles after autopicking was much lower than for datasets 1–3. This was owing to the generally lower quality of the γ-TuRC purification for this dataset and the smaller field of view—both resulting in a very low number of particles on each micrograph. To retrieve particles from the two subsets of data that could not be classified successfully using the standard approach, we added particles belonging to the high-quality 3D classes from the other two subsets as 'nucleators' for 3D classes with sufficient quality but removed them afterwards. Merged particles from all four subsets were subjected to two additional rounds of 3D classification to retrieve the final set of particles from dataset 4. These particles were extracted at 2.1 Å pixel size in boxes of 256 × 256 pixels and then processed identically to datasets 1–3.

A total of 46,096 polished particles from all four datasets were merged and subjected to 3D autorefinement, which then served as a basis for several rounds of 3D multibody refinement[29]. Using the cryo-EM density from 3D autorefinement, we prepared two sets of shape masks either (i) dividing the γ-TuRCs into seven dimers of successive spokes, or (ii) splitting the density into four segments, in which two segments represent the spoke 'heads' (C-terminal part of GRIP2 plus γ-tubulin) for spokes 1–7 and 8–14, respectively, and two segments represent the spoke 'base' (GRIP1 and N-terminal part of GRIP2) for spokes 1–7 and 8–14, respectively. All masks were generated by choosing an appropriate density threshold level for each density segment and extending the density envelope by 5 pixels and a soft edge of 5 pixels. Both sets of masks were used for a separate round of 3D multibody refinement. While 3D multibody refinement using the first set of masks resulted in much improved density for the spoke heads, the second set of masks yielded optimal refinement for the spoke bases. The resulting unfiltered density segments were merged into a composite map using UCSF Chimera[30]. Global resolution of the final density was estimated 4.9 Å; however, local resolution estimation indicated significantly lower resolution for dimers 2 (spokes 3/4) and 4 (spokes 7/8). To improve the density for these map segments, we subjected the particles to another round of 3D-multibody refinement, in which the respective dimers were split into independently refined monomers. Using this approach, we achieved improvement of the local resolution for these density segments, which improved the resolution globally to 4.8 Å.

All resolution estimates were performed according to the gold standard FSC criterion of independently refined half maps (FSC = 0.143) within RELION. Local resolution was estimated using the RELION local post-processing implementation. The *B*-factor value used during local resolution filtering was −300.

Grouping of γ-TuRC spokes into structural clusters

First, GCPs were clustered according to cross-correlation between density segments. The γ-TuRC density was segmented into 14 spokes, comprising one GCP plus one γ-tubulin each. Pairwise cross-correlation between these segments was then computed in UCSF Chimera using the Fit in the Map command taking into account all density voxels.

Second, GCPs were clustered according to the r.m.s.d. values of docked atomic models. The models for human GCP4 (PDB code 3RIP) and γ-tubulin (PDB code 1Z5W) were docked into all 14 spokes of the γ-TuRC density. The GCP4 atomic model was split into four rigid bodies to account for interdomain conformational flexibility: Met1–Lys147, Ile148–Tyr361, Leu362–Lys505 and Ser506–Gln636. The very C-terminal helix Ile637–Tyr654 was manually moved into the density for the first spoke and then kept rigid with the last segment for the other positions. Docked GCP4 and γ-tubulin models were then combined into one PDB file for each spoke and pairwise r.m.s.d. values were computed using the match command in UCSF Chimera. The average r.m.s.d. values computed between members of a specific cluster were at least two times smaller than the average r.m.s.d. values computed between members and nonmembers of a specific cluster (group (i): 0.75 Å versus 1.78 Å; group (ii): 0.60 Å versus 1.80 Å; group (iii) 1.61 Å versus 3.64 Å).

Identification of GCP-variant-specific structural features

Density segments covered by atomic models for GCP4 and γ-tubulin (prepared as described above) were annotated using the colour zone feature in UCSF Chimera. The remaining density segments for all spokes were compared against each other and correlated with primary sequence information on the different GCP variants guided by the docked GCP4 model, as described in the result section. Secondary structure prediction was performed in PSIPRED vs3.3[31,32] and multiple sequence alignment was performed in PROMALS[33].

Atomic modelling

The crystal structure of human GCP4 (PDB code 3RIP) was used as template for homology modelling of *X. laevis* GCPs on the Phyre2 web portal[34] with one-to-one threading. The following UniProt sequences were used: XP_018080012.1 (GCP2), O73787 (GCP3), Q642S3 (GCP4), XP_018102626.1 (GCP5) and Q9DDA7 (GCP6, excluding the insertion domain sequence Leu532–Arg1260). The crystal structure of human γ-tubulin (PDB code 1Z5W) was used as template for homology modelling of *X. laevis* γ-tubulin with UniProt sequence P23330. The homology models were subsequently docked into the γ-TuRC density map using UCSF Chimera. Each model was split into several rigid bodies to account for interdomain conformational flexibility. The rigid bodies consisted of: Leu209–G364, Tyr365–Glu506, Glu507–Ser668, Ser671–Ser714, Ala715–Tyr867 for GCP2; Glu246–Gly389, Arg390–Tyr552, Asn553–Lys691, Gly692–Tyr885 for GCP3; Met1–Lys147, Ile148–Asp349, Ile350–Lys505, Ser506–Tyr654 for GCP4; Thr259–Pro421, Asp422–Leu723, Leu724–Asn847 and Lys848–Ala1014 for GCP5; Gln269–Ala421, Gly422–Leu1015, Lys1016–Ser1464, Asn1465–Tyr1622 for GCP6. The last three C-terminal helices had to be manually positioned for all homology models, because their arrangement differed significantly in the X-ray structure. Missing or incorrectly localized segments of the homology models were appended or adjusted in Coot[35], where the density allowed. This includes Leu215–Cys209 and Thr605–Gly611 in GCP2; Leu791–Glu815, Val818–Ile839, Glu246–Ser248 in GCP3; Thr259–Gln265 and Arg571–Leu582 after removal of Arg571–Ser670 in GCP5; Gln269–Asp279 and Ser556–Met561 after removal of Phe532–Leu557 in GCP6. Unassigned, but clearly resolved, α-helices in the belt density were built as poly-alanine helices in Coot. In total, 17 helices were built with the following number of residues: 16, 19, 15, 13, 13, 17, 14, 15, 16, 16, 14, 13, 23, 15, 18, 13 and 31. Parts of the homology models not resolved in the cryo-EM reconstruction were removed. Rigid-body-fitted homology models were combined in Chimera into one model and main chain breaks caused by domainwise rigid-body fitting were repaired in Coot. The model was refined in real space against the cryo-EM density and structural clashes were removed using molecular dynamics flexible fitting (MDFF[36]). MDFF simulations were prepared using QwikMD[37] and carried out with NAMD[38] using the CHARMM36 force field. Secondary structure, *cis* peptide and chirality restraints were used during 800 steps of minimization followed by a 40-ps simulation at 300 K. The resulting model was refined in Phenix 1.14 using the initial model as reference and then submitted to the NAMDinator website tool[39] that combines molecular dynamics flexible fitting (MDFF) with real-space refinement in Phenix. MDFF was performed at 298 K using 2,000 minimization steps and 20,000 simulation steps. Simulation was run in vacuo with scaling factor of 0.3. Subsequently, the fit of resolved bulky amino acid side chains was inspected and corrected in Coot, if required, before the model was refined in Phenix. This procedure was repeated twice with two slightly different refinement parameters to

obtain the final model. Model validation was performed in Phenix 1.14[40]. The register of the atomic model was confirmed by the following list of resolved bulky amino acid side chains (spoke number/residue/unique as defined in Extended Data Fig. 5): 1/His359/-, 1/Tyr377/-, 1/Tyr455/*, 1/His725/-, 3/Phe275/, 3/Trp324/*, 3/Tyr455/*, 3/His724/-, 5/Trp324/**, 5/Phe325/**, 5/Arg486/-, 5/Tyr493/-, 5/Phe501/-, 5/His643/-, 5/Tyr646/*, 5/His649/-, 5/His724/-, 7/His289/-, 7/Trp324/*, 7/His359/**, 7/Phe363/**, 7/Tyr455/*, 7/Tyr491/-, 7/His511/-, 7/Trp705/-, 13/Phe275/-, 13/Trp324/*, 13/His359/-, 2/Trp298/-, 2/His386/-, 2/His658/*, 2/Phe665/-, 4/Trp298/-, 4/Phe369/**, 4/Phe371/**, 4/His416/-, 4/Trp667/-, 6/Trp298/-, 6/His342/-, 6/Phe369/-, 6/Trp371/-, 6/Tyr423/*, 6/Phe491/*, 6/Phe529/-, 6/Phe538/-, 6/Phe665/-, 6/Trp680/-, 10/Phe371/*, 10/His409/*, 10/Tyr437/-, 10/Phe458/**, 10/Trp461/**, 10/Tyr703/-, 10/Tyr816/-, 10/Phe820/-, 8/Trp298/-, 8/Tyr306/-, 8/Phe323/-, 8/Tyr334/**, 8/Tyr335/**, 8/His342/-, 8/Phe371/-, 8/His386/-, 8/His416/-, 8/Tyr423/*, 8/Phe529/-, 8/Tyr543/*, 8/His557/-, 8/Tyr719/-, 8/His750/-, 8/His851/-, 14/Trp298/-, 14/Tyr402/-, 14/His493/-, 14/Tyr 537/-, 14/Phe538/-, 14/Phe852/-, 9/Lys47/*, 9/Arg54/-, 9/Phe55/**, 9/Phe58/**, 9/Tyr124/-, 9/Phe129/-, 9/Tyr158/-, 9/Tyr184/-, 9/His390/-, 9/His401/-, 9/Phe478/-, 9/His 560/-, 9/His562/*, 9/His580/*, 9/His590/*, 11/Phe58/*, 11/His121/*, 11/His130/*, 11/Tyr158/-, 11/Tyr184/-, 11/Trp190/-, 10/Trp272/-, 10/Tyr316/-, 10/Trp362/*, 10/Phe368/-, 10/His925/-, 10/His933/*, 12/His340/-, 12/Tyr367/-, 12/Tyr400/*, 12/Tyr431/**, 12/Tyr433/**.

Unbiased structure-guided identification approach

For the list of proteins identified in the purified γ-TuRC by LFQ mass spectrometry, we either downloaded X-ray structures from the PDB or—where possible—prepared high-confidence homology models in HHpred. Subsequently, the fitmap command of UCSF Chimera was used to fit these atomic models into the envelope of the cryo-EM density, starting from 10,000 randomly sampled starting positions and orientations for each model. The following parameters were used: correlation metric with simulated densities at 6 Å resolution, 50 Å radius around the starting position, global search. For each relevant model, the number of fits was plotted against the respective cross-correlation coefficients (Extended Data Fig. 6). Atomic models for NEDD1, NME7 and MOZART1 were limited to protein segments with high homology to known structures (1–361 for NEDD1; 26–58 for MOZART1; 91–226 and 235–373 for NME7). The following list of proteins could not be localized in the γ-TuRC density even though highly abundant in the γ-TuRC purification according to LFQ mass spectrometry (UniProt code/protein name/template probability from homology modelling/LFQ intensity): A0A1L8H345/dynamin-1/100/8.72E+09, Q8AVE2/Hsc70 protein/100/5.89E+09, A0A1L8FKY3/Hsp70/100/5.5E+09, A0A1L8HW84/tight junction protein ZO-3/100/5.47E+09, Q7ZTN1/tight junction protein ZO-3/100/5.42E+09, A0A1L8GWY3/protein transport protein Sec24a/100/5.26E+09, A0A1L8FW10/insulin-like growth factor 2 mRNA-binding protein 3/99.95/4.34E+09, A0A1L8EKZ2/polyadenylate-binding protein/100/4.32E+09, A0A1L8G1U5/protein transport protein SEC23/100/3.92E+09, A0A1L8ES55/polyadenylate-binding protein/100/3.72E+09, A0A1L8H4P1/CSD_1 domain-containing protein/99.35/3.36E+09, A0A1L8G7U0/protein transport protein SEC23/100/2.75E+09, A0A1L8GRB6/uncharacterized protein/100/2.47E+09, A0A1L8GY92/ WD_REPEATS_REGION domain-containing protein/99.96/1.77E+09, A0A1L8HEX9/uncharacterized protein/100/1.67E+09, A0A1L8FA78/heat shock-related 70 kDa protein; signalling protein/100/1.62E+09, A0A1L8F1H5/dynamin-1/100/1.47E+09, A0A1L8HWC1/uncharacterized protein/100/1.45E+09, A0A1L8GMZ9/dynamin-1/100/1.39E+09, Q8AVK9/NSEP1 protein/99.33/1.15E+09, A0A1L8F457/protein transport protein SEC23/100/1.07E+09, A0A1L8FAZ8/protein transport protein SEC23/100/1.01E+09, A0A1L8GWQ5/WD repeats region domain-containing protein/100/8.22E+08, A0A1L8HF79/nucleoside diphosphate kinase 7/99.92/7.27E+08, A0A1L8G3Y8/fragile X mental retardation syndrome-related protein 1/100/7.13E+08, A3KMH8/fragile X mental retardation syndrome-related protein 1/100/7.11E+08, A0A1L8EWC9/interferon-inducible double-stranded RNA-dependent protein kinase activator A/100/6.98E+08, A0A1L8FKW5/serine/threonine-protein kinase TOR/100/6.7E+08, A0A1L8F6I3/HSPA5 protein/100/6.64E+08, A0A1L8GQQ7/uncharacterized protein/100/5.84E+08, A0A1L8HM56/protein transport protein Sec24B/100/5.23E+08, A0A1L8FTJ1/polyadenylate-binding protein/100/4.81E+08, A0A1L8FZR3/polyadenylate-binding protein/100/4.81E+08, A0A1L8EM44/γ-actin/ 100/4.77E+08, A0A1L8ETE5/uncharacterized protein/100/4.77E+08, A0A1L8HRT0/DZF domain-containing protein/100/4.46E+08, A0A1L8GT63/tight junction protein ZO-1/100/4.42E+08, Q6GMC1/ubiquitin-40S ribosomal protein S27a/100/4.27E+08, A0A1L8G5V1/ubiquitin-like domain-containing protein/100/4.27E+08, A0A1L8HQK4/ polyubiquitin-C/100/4.26E+08, Q7SY79/Ubc-prov protein/100/4.26E+08, Q6GQF3/ ubiquitin-60S ribosomal protein L40/100/4.26E+08, A0A1L8HX68/ubiquitin-like domain-containing protein/99.94/4.26E+08, A0A1L8HCZ9/uncharacterized protein/100/4.26E+08, A0A1L8H6E1/nucleoside diphosphate kinase 7/99.92/4.13E+08.

Analysis of geometrical parameters

For analysis of geometrical parameters of the γ-TuRC, we first computed the (approximate) helical axis for each of the analysed models by fitting a straight line through the centroids described below. For the γ-TuRC, we defined centroids for five different sets of atoms along the spokes (Fig. 4a) using UCSF Chimera. Two points were defined on the γ-tubulin subunit of each spoke (γ-tubulin Thr145, γ-tubulin Tyr152), while the other three points were defined based on aligned amino acids of the GCPs (point 1: Leu554 of GCP3, Leu508 of GCP2, Met590 of GCP6, Leu350 of GCP4, Leu711 of GCP5; point 2: Pro408 of GCP3, Ser369 of GCP2, Tyr445 of GCP6, Pro166 of GCP4, Glu451 of GCP5; point 3: Leu249 of GCP3, Leu216 of GCP2, Met1 of GCP4, Val266 of GCP5, Leu280 of GCP6). For the 13-spoked MT (based on PDB 6EVZ), three centroids were defined based on Gln15 of three different layers in the MT. For the yeast γ-TuSC in the closed conformation (PDB 5FLZ), three centroids were defined based on yeast γ-tubulin Gln12, Asn389 of GCP2/Asn444 of GCP3 and Phe102 of GCP2/Phe216 of GCP3. All three models were subsequently aligned according to their central axis and coordinates were transformed such that the axes correspond to the *z*-axis of the coordinate system. Cartesian coordinates of tubulins were determined based on conserved residues (Gln15, Gln16 and His16). On the basis of these coordinates, we computed the pitch (Fig. 4b) for each spoke and radial distances (Fig. 4c).

Using UCSF Chimera, refined homology models for GCPs and γ-tubulins (see above) were docked as rigid bodies into the cryo-EM density of the yeast γ-TuSC oligomer in a closed conformation (EMD-2799). The atomic models of the *X. laevis* γ-TuRC in the experimentally observed conformation and the simulated closed conformation were aligned with respect to spoke 1 using UCSF Chimera. The conformational changes linking both models were captured in motion by interpolating between the two conformations using UCSF Chimera's morph conformations function. In an alternative approach to visualize the conformational change, we used PyMol[41] to draw vectors between Cα atoms in the two conformations and colour-coded them according to their r.m.s.d. values.

To analyse relative GRIP1–GRIP2 domain inclinations, we computed their axes for each spoke. To define the GRIP1 domain axis, we used the following corresponding residue pairs: Ala266/Gly453 for GCP2, Gly297/Gly486 for GCP3, Gly49/Gly280 for GCP4, Gly317/Gly559 for GCP5 and Gly332/Gly526 for GCP6. To define the GRIP2 domain axis, we used the following corresponding residue pairs: Leu508/Phe757 for GCP2, Leu554/Phe784 for GCP3, Leu350/Phe592 forGCP4, Leu711/Phe959 for GCP5 and Met1319/Phe1553 for GCP6. The relative inclinations of GRIP1 and GRIP2 domains were measured in UCSF Chimera with the angle command. The GRIP1–GRIP2 inclinations were computed separately for each spoke and then quantified for each GCP

variant: five copies of GCP2, five copies of GCP3, two copies of GCP4, one copy of GCP5 and one copy of GCP6. The average angle for each GCP group was calculated as mean ± s.e.m.

To analyse interspoke distances, we computed distances between conserved residues in the GCP GRIP1 and GRIP2 domains or γ-tubulins of neighbouring spokes in UCSF Chimera. The following residues were used: Ala266 of GCP2, Gly297 of GCP3, Gly49 of GCP4, Gly317 of GCP5 and Gly332 of GCP6 for the GRIP1 domain; Phe757 of GCP2, Phe784 of GCP3, Phe592 of GCP4, Phe959 of GCP5 and Phe1553 of GCP6 for the GRIP2 domain; Asn187 for γ-tubulin.

Research animals

The permission numbers for *X. laevis* experiment are: 35-9185.81/G-204/12 (Regierungspräsidium Karlsruhe, BW); 81-02.05.40.17.091 (LANUF Recklinghausen, NRW). Ethic justification of the experiment is according to § 7a Abs. 2 Nr. 3 TierSchG. We have complied with all relevant ethical regulations. The injection of hormones into frogs mimics the physiological stimulus upon reproduction with a negligible burden for animals. In turn, the experiments in *X. laevis* using laid eggs and derived extracts have contributed ground-breaking knowledge to basic mechanisms of cell division, cell cycle control and MT functions. The latter has led, for example, to the discovery and characterization of cytostatic drugs such as taxol (Paclitaxel). These experiments are therefore performed with an optimal cost–benefit ratio, and show hardly any harm to animals while allowing great potential for gaining knowledge for basic and applied science.

Reporting summary

Further information on research design is available in the Nature Research Reporting Summary linked to this paper.

Data availability

Cryo-EM densities of the γ-TuRC filtered according to global or local resolution have been deposited in the Electron Microscopy Data Bank (EMDB) under accession code EMD-10491. Atomic coordinates for the γ-TuRC have been deposited at the PDB under accession code 6TF9. The original immunoblots and further source data from LFQ mass spectrometry (Fig. 2a), immunoblot quantification (Fig. 3c), geometric analysis of the atomic model (Figs. 3g, 4b–d), MT nucleation assays (Extended Data Figs. 1c, 6i, 9b, d), circular dichroism measurements (Extended Data Fig. 4e), unbiased structure-guided identification (Extended Data Fig. 6a–d), quantification of indirect immunofluorescence (Extended Data Fig. 6g) and actin polymerization (Extended Data Fig. 6h) are included in the Supplementary Information. The raw cryo-EM micrograph movie stacks are available from the corresponding authors upon request.

16. Zhang, L., Keating, T. J., Wilde, A., Borisy, G. G. & Zheng, Y. The role of Xgrip210 in γ-tubulin ring complex assembly and centrosome recruitment. *J. Cell Biol*. **151**, 1525–1536 (2000).
17. Chinen, T. et al. The γ-tubulin-specific inhibitor gatastatin reveals temporal requirements of microtubule nucleation during the cell cycle. *Nat. Commun*. **6**, 8722 (2015).
18. Bärenz, F. et al. The centriolar satellite protein SSX2IP promotes centrosome maturation. *J. Cell Biol*. **202**, 81–95 (2013).
19. Cox, J. & Mann, M. MaxQuant enables high peptide identification rates, individualized p.p.b.-range mass accuracies and proteome-wide protein quantification. *Nat. Biotechnol*. **26**, 1367–1372 (2008).
20. Schwanhäusser, B. et al. Global quantification of mammalian gene expression control. *Nature* **473**, 337–342 (2011).
21. Tang, G. et al. EMAN2: an extensible image processing suite for electron microscopy. *J. Struct. Biol*. **157**, 38–46 (2007).
22. van Heel, M., Harauz, G., Orlova, E. V., Schmidt, R. & Schatz, M. A new generation of the IMAGIC image processing system. *J. Struct. Biol*. **116**, 17–24 (1996).
23. Liu, X. & Wang, H. W. Single particle electron microscopy reconstruction of the exosome complex using the random conical tilt method. *J. Vis. Exp*. **49**, 2574 (2011).
24. Mastronarde, D. N. Automated electron microscope tomography using robust prediction of specimen movements. *J. Struct. Biol*. **152**, 36–51 (2005).
25. Zivanov, J. et al. New tools for automated high-resolution cryo-EM structure determination in RELION-3. *eLife* **7**, e42166 (2018).
26. Zheng, S. Q. et al. MotionCor2: anisotropic correction of beam-induced motion for improved cryo-electron microscopy. *Nat. Methods* **14**, 331–332 (2017).
27. Zhang, K. Gctf: Real-time CTF determination and correction. *J. Struct. Biol*. **193**, 1–12 (2016).
28. Zivanov, J., Nakane, T. & Scheres, S. H. W. A Bayesian approach to beam-induced motion correction in cryo-EM single-particle analysis. *IUCrJ*. **6**, 5–17 (2019).
29. Nakane, T., Kimanius, D., Lindahl, E. & Scheres, S. H. W. Characterisation of molecular motions in cryo-EM single-particle data by multi-body refinement in RELION. *eLife* **7**, e36861 (2018).
30. Pettersen, E. F. et al. UCSF Chimera—a visualization system for exploratory research and analysis. *J. Comput. Chem*. **25**, 1605–1612 (2004).
31. Buchan, D. W. A. & Jones, D. T. The PSIPRED Protein Analysis Workbench: 20 years on. *Nucleic Acids Res*. **47**, W402–W407 (2019).
32. Jones, D. T. Protein secondary structure prediction based on position-specific scoring matrices. *J. Mol. Biol*. **292**, 195–202 (1999).
33. Pei, J., Tang, M. & Grishin, N. V. PROMALS3D web server for accurate multiple protein sequence and structure alignments. *Nucleic Acids Res*. **36**, W30–W34 (2008).
34. Kelley, L. A., Mezulis, S., Yates, C. M., Wass, M. N. & Sternberg, M. J. The Phyre2 web portal for protein modeling, prediction and analysis. *Nat. Protocols* **10**, 845–858 (2015).
35. Emsley, P., Lohkamp, B., Scott, W. G. & Cowtan, K. Features and development of Coot. *Acta Crystallogr. D* **66**, 486–501 (2010).
36. Trabuco, L. G., Villa, E., Schreiner, E., Harrison, C. B. & Schulten, K. Molecular dynamics flexible fitting: a practical guide to combine cryo-electron microscopy and X-ray crystallography. *Methods* **49**, 174–180 (2009).
37. Ribeiro, J. V. et al. QwikMD — integrative molecular dynamics toolkit for novices and experts. *Sci. Rep*. **6**, 26536 (2016).
38. Phillips, J. C. et al. Scalable molecular dynamics with NAMD. *J. Comput. Chem*. **26**, 1781–1802 (2005).
39. Kidmose, R. T. et al. *Namdinator* - automatic molecular dynamics flexible fitting of structural models into cryo-EM and crystallography experimental maps. *IUCrJ*. **6**, 526–531 (2019).
40. Adams, P. D. et al. PHENIX: a comprehensive Python-based system for macromolecular structure solution. *Acta Crystallogr. D* **66**, 213–221 (2010).
41. Delano, W. L. PyMOL: an open-source molecular graphics tool http://www.ccp4.ac.uk/newsletters/newsletter40/11_pymol.pdf (2018).
42. Waterhouse, A. M., Procter, J. B., Martin, D. M., Clamp, M. & Barton, G. J. Jalview Version 2—a multiple sequence alignment editor and analysis workbench. *Bioinformatics* **25**, 1189–1191 (2009).
43. Sievers, F. & Higgins, D. G. Clustal Omega for making accurate alignments of many protein sequences. *Protein Sci*. **27**, 135–145 (2018).
44. Sievers, F. et al. Fast, scalable generation of high-quality protein multiple sequence alignments using Clustal Omega. *Mol. Syst. Biol*. **7**, 539 (2011).

Acknowledgements We thank A. Boland for graphene oxide grids, G. Hofhaus and T. Mielke for technical cryo-EM support, S. Hata for suggestions, S. Kmiecik for assisting with circular dichroism measurements, L. Rohland for assisting with circular dichroism and actin polymerization measurements. We acknowledge the services SDS@hd and bwHPC supported by the Ministry of Science, Research and the Arts Baden-Württemberg, as well as the German Research Foundation (INST 35/1314-1 FUGG and INST 35/1134-1 FUGG). We also acknowledge support from the German Research Foundation to E.S. (Schi 295/4-3), O.J.G. (GR-1737/9-1) and T. Ruppert (Ru 747/1-1). P.L. received a HBIGS fellowship.

Author contributions P.L. optimized γ-TuRC purification, performed γ-TuRC activity measurements, salt treatments, CEP215-N analyses in vitro and in egg extracts, GCP6 insertion domain alignment, sucrose gradient and silver staining. P.L. and A.N. performed negative-stain electron microscopy and particle selection. E.S. and P.L. performed the DNaseI inhibition experiment. D.F. performed 2D classification of negatively stained γ-TuRC. J.L. and C.S. performed initial cryo-EM analysis of the γ-TuRC. P.L. and A.N. prepared, optimized and screened γ-TuRC cryo-EM grids and, together with E.Z., selected particles for initial model generation. P.L. performed immunoprecipitation experiments. A.B. performed circular dichroism measurements and actin polymerization assay. T. Ruppert performed LFQ mass spectrometry analysis. A.N. and A.B. detected actin in the γ-TuRC by immunofluorescence. C.P. prepared egg extracts. O.J.G. provided egg extracts and advised P.L. with the γ-TuRC purification. E.Z. analysed the negative-staining data of γ-TuRC and CEP215-N, acquired and analysed cryo-EM data, and, together with T. Rudack, prepared atomic models and pursued all related aspects of structure analysis. All authors discussed and interpreted the γ-TuRC cryo-EM density. E.S. and S.P. planned and supervised the experiments, analysed data and, together with E.Z. and P.L., wrote the manuscript.

Competing interests The authors declare no competing interests.

Additional information

Supplementary information is available for this paper at https://doi.org/10.1038/s41586-019-1896-6.

Correspondence and requests for materials should be addressed to S.P. or E.S.

Reprints and permissions information is available at http://www.nature.com/reprints.

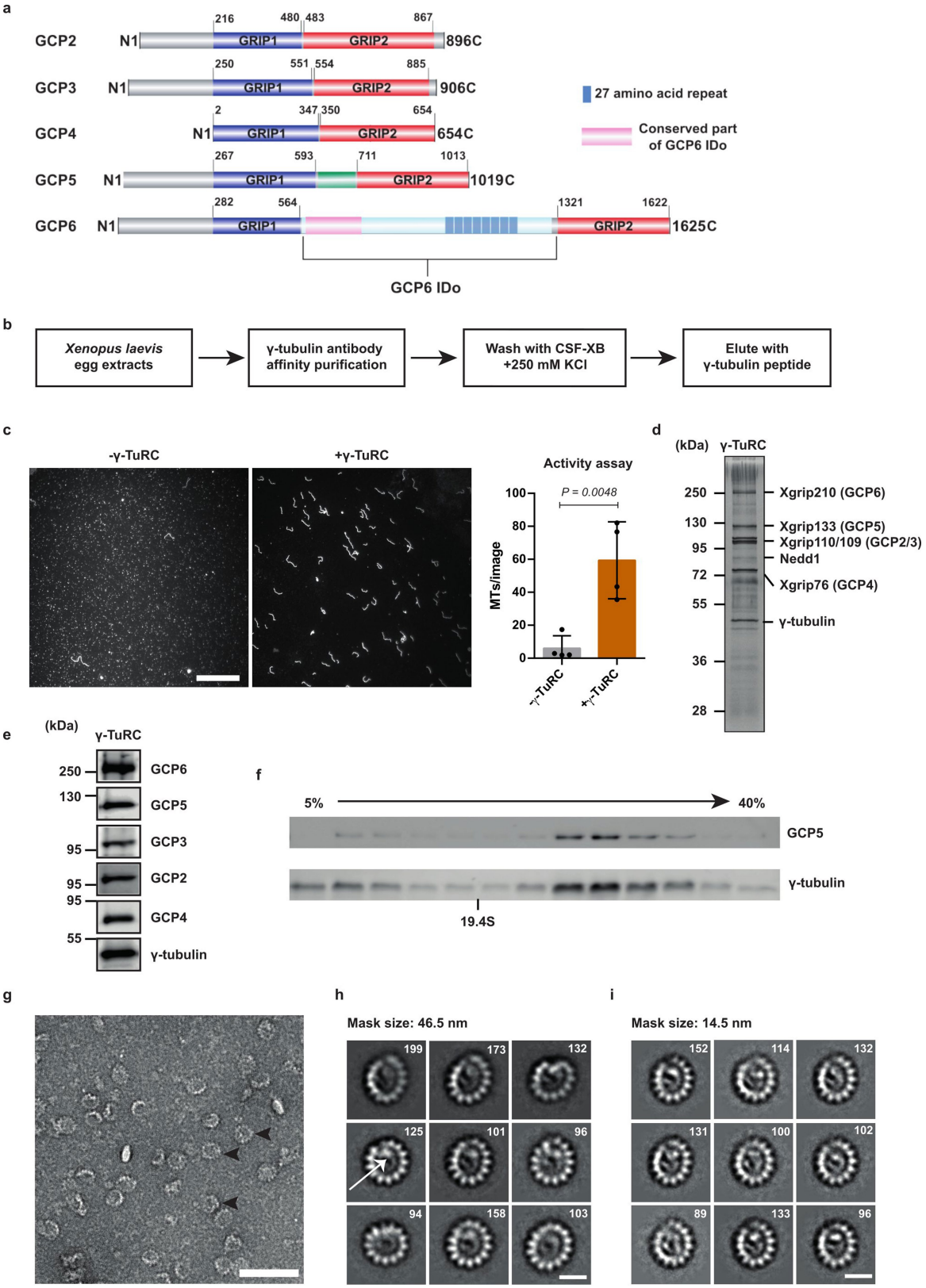

Extended Data Fig. 1 | See next page for caption.

Extended Data Fig. 1 | Biochemical, functional and structural characterization of γ-TuRCs purified from *X. laevis* egg extracts. a, Domain organization of GCP2–GCP6. Between the conserved GRIP1 and GRIP2 domains, GCP5 and GCP6 possess a 120- and 750-residue-long insertion domain, respectively. The GCP6 insertion domain contains 8 repeats of 27 amino acids. Domains are annotated according to the Pfam database. **b**, Schematic of γ-TuRC purification. The γ-TuRC was purified with γ-tubulin antibody-crosslinked Protein A Dynabeads, washed with CSF-XB buffer containing 250 mM salt (KCl), and then eluted by a short peptide corresponding to the C terminus of γ-tubulin. **c**, Purified γ-TuRCs showed basal MT nucleation activity. Experiment was carried out with (+) or without (–) purified γ-TuRCs, and 33 µM tubulin (5% Cy3-labelled tubulin for visualization). In the negative control, the same purification procedure was used with eluates from rabbit random IgG-crosslinked Protein A Dynabeads. Twenty random images were acquired with a light microscope, and representative overview images are shown. Right, the number of MTs was quantified by ImageJ and data are mean ± s.d. $n = 4$ biologically independent experiments. P value determined by unpaired two-sided t-test. Scale bar, 10 µm. **d**, **e**, After the affinity purification of γ-TuRCs, the eluted proteins were resolved by SDS–PAGE followed by silver staining (**d**) and immunoblotting (**e**). Representative images in **d** and **e** are from three biologically independent experiments. For gel source data, see Supplementary Fig. 1. **f**, Immunoblotting analysis of the purified γ-TuRCs after sucrose gradient. Purified γ-TuRCs were applied to a 5–40% sucrose gradient and fractionated after centrifugation. Fractions were resolved by SDS–PAGE and probed using γ-tubulin and GCP5 antibodies. Thyroglobulin (19.4 S) was used as a standard marker and run on a parallel gradient. Representative images were from three biologically independent experiments. For gel source data, see Supplementary Fig. 1. **g**, Confirmation of structural integrity of the purified γ-TuRCs by negative-staining electron microscopy. Representative micrograph is from five biologically independent experiments. Scale bar, 100 nm. Black arrowheads denote examples of particles used in 2D classification and averaging. **h**, **i**, γ-TuRC particles from the negative-stain electron microscopy were classified and averaged with a mask size of either 46.5 nm (**h**) or 14.5 nm (**i**). Representative classes of γ-TuRCs are from three biologically independent experiments. The number of particles contributing to each class is given. An example of the 'asymmetric' density inside the γ-TuRC is highlighted by a white arrow (**h**), which is more readily visible with a 14.5-nm mask focusing on the inner part of the γ-TuRC (**i**). Scale bars, 20 nm.

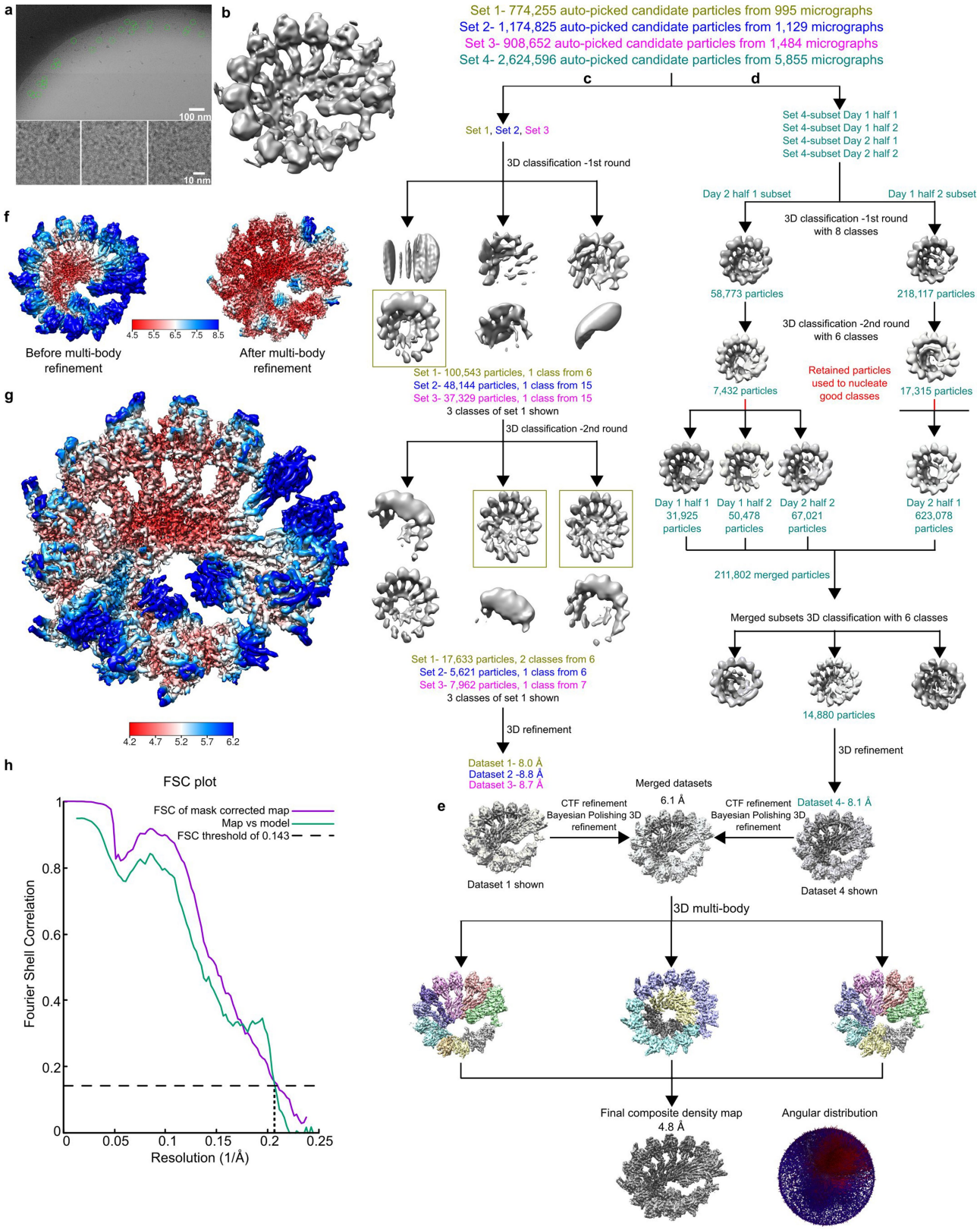

Extended Data Fig. 2 | See next page for caption.

Extended Data Fig. 2 | Cryo-EM data processing and resolution estimation. **a**, A representative micrograph from four biologically independent experiments with manually selected particles (green circles) is shown. Three selected particles are shown below. **b**, Initial model of the γ-TuRC obtained from 3,000 manually selected particles (Methods). Scale bars are depicted in **a**. **c**, Four datasets were acquired and initially processed separately. Datasets 1, 2 and 3 were submitted to two consecutive rounds of 3D classification with a varying number of classes. All class averages obtained for dataset 1 are shown. Retained class averages are highlighted by a rectangular box. **d**, Dataset 4 was the largest dataset, and was therefore divided into four subsets. The higher-quality subsets were submitted to two rounds of 3D classification and particles encompassed in the high-quality classes from these two subsets were combined with all four original subsets of particles to nucleate high-quality classes in the two lower-quality subsets. Only class averages retained for further processing are shown. **e**, The final sets of particles from all four datasets were refined separately, submitted to CTF refinement and Bayesian polishing, and subsequently merged. The γ-TuRC density was split into several combinations of segments, as indicated. All combinations of segments were subjected to a multibody 3D refinement separately. Their output density segments were combined into one composite density for analysis. The angular distribution of particle views is shown. **f**, Comparison of local resolution estimation before (left) and after (right) 3D multibody refinement. Local resolution was markedly improved for the peripheral segments of the γ-TuRC density reconstruction upon 3D multibody refinement. The colour-coded resolution scale is identical for both panels. **g**, Local resolution estimation of the final γ-TuRC density map with a resolution range covering the entire spectrum. **h**, Mask-corrected FSC between the two independently refined half-set reconstructions (purple), and between the full reconstruction and the atomic model for the γ-TuRC (green).

a Cross correlation of EM density segments

	Spoke 1	Spoke 2	Spoke 3	Spoke 4	Spoke 5	Spoke 6	Spoke 7	Spoke 8	Spoke 9	Spoke 10	Spoke 11	Spoke 12	Spoke 13	Spoke 14
Spoke 1	0.96	0.90	0.92	0.90	0.92	0.90	0.92	0.89	0.87	0.87	0.85	0.87	0.92	0.89
Spoke 2	0.89	0.97	0.88	0.93	0.88	0.93	0.88	0.93	0.83	0.87	0.82	0.88	0.88	0.93
Spoke 3	0.93	0.89	0.96	0.89	0.93	0.89	0.93	0.87	0.87	0.86	0.84	0.87	0.92	0.88
Spoke 4	0.90	0.94	0.89	0.97	0.90	0.94	0.90	0.93	0.85	0.89	0.82	0.88	0.89	0.93
Spoke 5	0.93	0.89	0.93	0.90	0.96	0.90	0.93	0.89	0.88	0.87	0.86	0.88	0.92	0.89
Spoke 6	0.89	0.93	0.89	0.93	0.89	0.96	0.90	0.93	0.84	0.88	0.81	0.88	0.89	0.92
Spoke 7	0.93	0.90	0.93	0.91	0.94	0.91	0.97	0.90	0.88	0.88	0.86	0.88	0.93	0.90
Spoke 8	0.89	0.93	0.88	0.93	0.89	0.93	0.89	0.97	0.85	0.89	0.83	0.88	0.89	0.93
Spoke 9	0.88	0.86	0.89	0.86	0.89	0.87	0.88	0.86	0.96	0.86	0.90	0.86	0.88	0.85
Spoke 10	0.86	0.87	0.86	0.87	0.86	0.88	0.87	0.88	0.84	0.96	0.84	0.87	0.86	0.87
Spoke 11	0.85	0.84	0.86	0.85	0.86	0.85	0.85	0.84	0.90	0.85	0.96	0.86	0.85	0.85
Spoke 12	0.85	0.86	0.86	0.86	0.85	0.86	0.85	0.86	0.82	0.86	0.84	0.96	0.86	0.85
Spoke 13	0.92	0.89	0.92	0.89	0.92	0.90	0.92	0.89	0.87	0.87	0.85	0.88	0.96	0.89
Spoke 14	0.88	0.93	0.88	0.93	0.88	0.93	0.88	0.93	0.83	0.88	0.83	0.88	0.89	0.97

b RMSD between fitted atomic models

	Spoke 1	Spoke 2	Spoke 3	Spoke 4	Spoke 5	Spoke 6	Spoke 7	Spoke 8	Spoke 9	Spoke 10	Spoke 11	Spoke 12	Spoke 13	Spoke 14
Spoke 1	0	1.736	0.756	1.572	0.688	1.551	0.638	1.87	2.588	2.477	3.634	2.138	1.2	1.932
Spoke 2	1.736	0	2.188	0.51	1.899	0.536	1.838	0.626	3.765	1.909	4.729	1.462	1.935	0.712
Spoke 3	0.756	2.188	0	2.008	0.471	1.922	0.591	2.259	2.383	2.639	3.457	2.333	0.946	2.269
Spoke 4	1.572	0.51	2.008	0	1.72	0.366	1.632	0.688	3.656	1.952	4.614	1.378	1.767	0.746
Spoke 5	0.688	1.899	0.471	1.72	0	1.633	0.53	1.953	2.494	2.361	3.6	2.073	0.75	1.951
Spoke 6	1.551	0.536	1.922	0.366	1.633	0	1.565	0.567	3.557	1.727	4.548	1.35	1.602	0.612
Spoke 7	0.638	1.838	0.591	1.632	0.53	1.565	0	1.903	2.715	2.376	3.815	2.046	0.91	1.864
Spoke 8	1.87	0.626	2.259	0.688	1.953	0.567	1.903	0	3.868	1.709	4.879	1.531	1.932	0.622
Spoke 9	2.588	3.765	2.383	3.656	2.494	3.557	2.715	3.868	0	3.928	1.61	3.689	2.781	3.94
Spoke 10	2.477	1.909	2.639	1.952	2.361	1.727	2.376	1.709	3.928	0	5.08	1.892	2.136	1.625
Spoke 11	3.634	4.729	3.457	4.614	3.6	4.548	3.815	4.879	1.61	5.08	0	4.695	3.89	5.007
Spoke 12	2.138	1.462	2.333	1.378	2.073	1.35	2.046	1.531	3.689	1.892	4.695	0	2.06	1.423
Spoke 13	1.2	1.935	0.946	1.767	0.75	1.602	0.91	1.932	2.781	2.136	3.89	2.06	0	1.819
Spoke 14	1.932	0.712	2.269	0.746	1.951	0.612	1.864	0.622	3.94	1.625	5.007	1.423	1.819	0

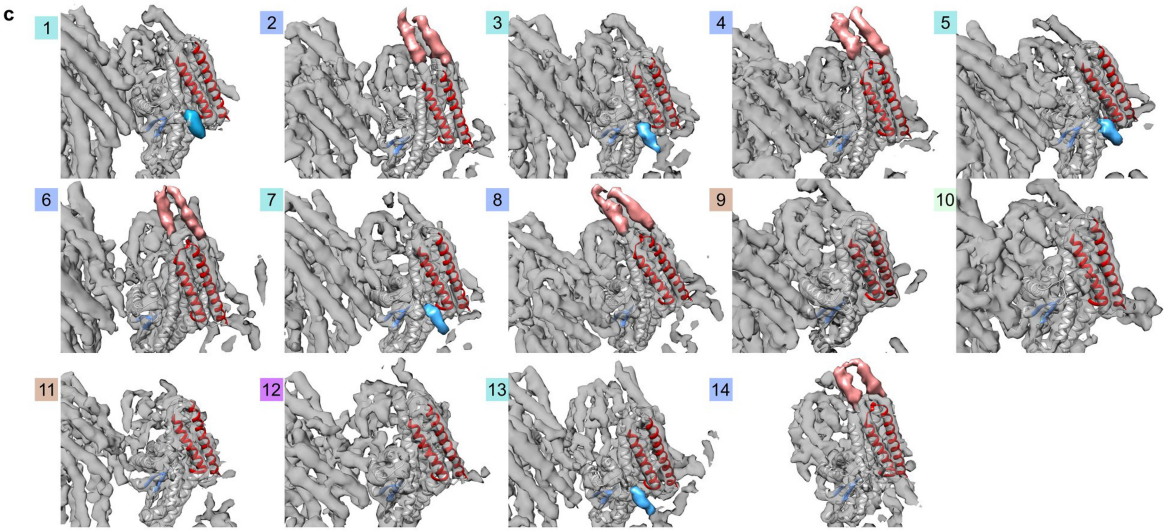

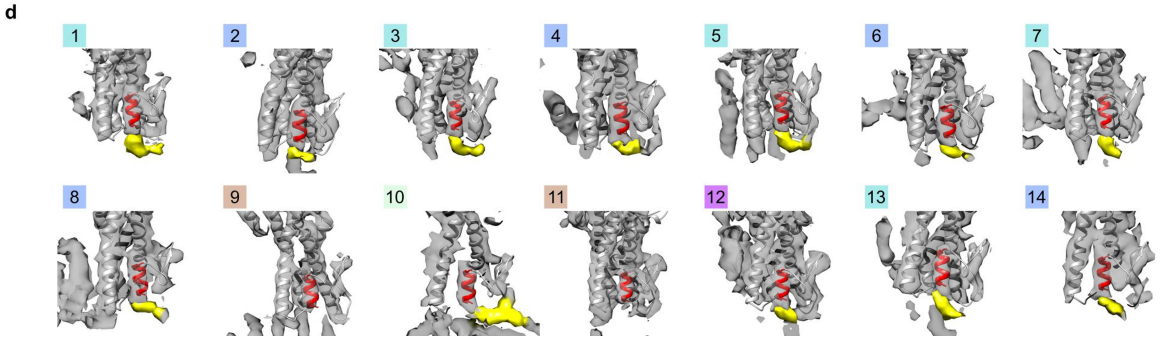

Extended Data Fig. 3 | See next page for caption.

Extended Data Fig. 3 | Structural grouping and unique GCP-variant-specific features identify GCP proteins in the γ-TuRC. a, Pairwise cross-correlation between isolated density segments, colour-coded from higher (red) to lower (blue) correlation. The actual correlation values are given. **b**, Atomic models of human GCP4 and γ-tubulin were fitted into the 14 γ-TuRC spokes domainwise (Methods). Pairwise r.m.s.d. between Cα atoms of atomic models representing the individual spokes, colour-coded from lower (red) to higher (blue) r.m.s.d. values. The actual r.m.s.d. values are given. Both approaches cluster the spokes into five classes, colour-coded in the left column and top row. **c**, **d**, Atomic models for human GCP4 (white) were fitted domainwise into the density. Density segments covered by the atomic model are depicted in transparent grey. Remaining unexplained segments are depicted in colour. Features are shown for all 14 individual spokes of the γ-TuRC. **c**, Characteristic density segments of the GRIP2 domain. Extended C-terminal α-helices (red model and density) are unique for group (ii) (spokes 2, 4, 6, 8, 14), and an extended loop between the GRIP2 β-strands (blue model and density) is present only in group (i) (spokes 1, 3, 5, 7, 13). **d**, Unexplained density segments N-terminal of the GRIP1 domain. Only group (iii) (spokes 9, 11) is devoid of a continuous density connecting to the N-terminal helix of GCP4 (position 9 and 11; lack of yellow extension). Colour code as in Fig. 1a.

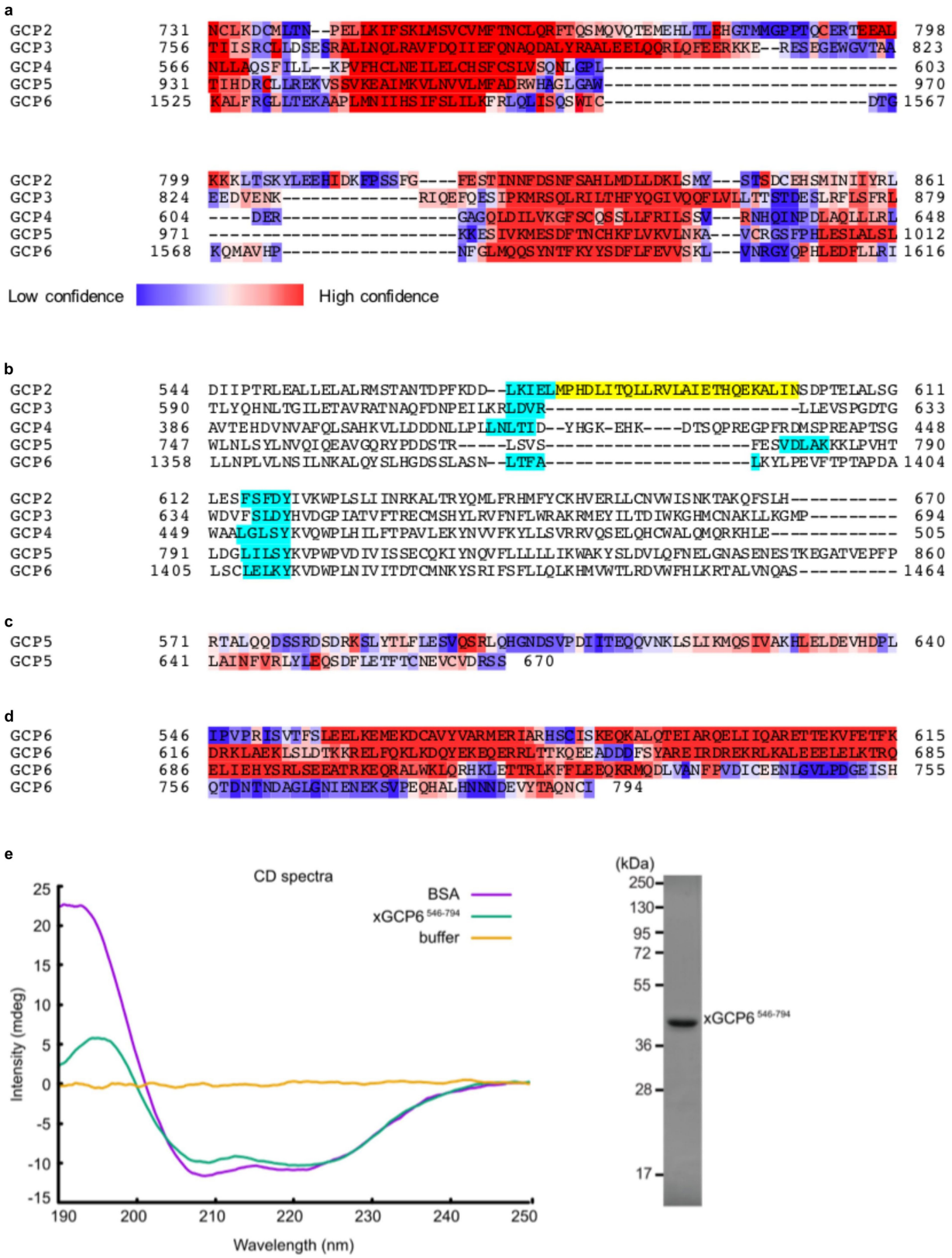

Extended Data Fig. 4 | See next page for caption.

Extended Data Fig. 4 | Secondary structure prediction and biochemical characterization for GCP variant-distinguishing regions and the GCP5 and GCP6 insertion domains. a, C-terminal segments of all GCP variants were aligned and the secondary structure was predicted. Confidence for α-helical secondary structure is colour-coded (blue denotes low confidence, red denotes high confidence). **b**, Multiple sequence alignment for the GRIP2 segments encompassing the inter-β-strand loop for all GCP variants. β-strands are highlighted in blue. **c**, Secondary structure prediction for the insertion domain of GCP5. The prediction confidence for α-helical secondary structure is colour-coded. **d**, Secondary structure prediction of xGCP6(546–794) showing highly α-helical character. **e**, Circular dichroism (CD) analysis of the purified xGCP6(546–794). Left, representative plots are from three biologically independent experiments. Comparison of the circular dichroism spectra for xGCP6(546–794) and BSA (containing only α-helices) confirms the predicted α-helical character of the N-terminal part of the GCP6 insertion domain. Right, Coomassie-blue-stained SDS–PAGE gel of the elution fraction of the xGCP6(546–794) shows the purity of the sample. Representative image is from three biologically independent experiments.

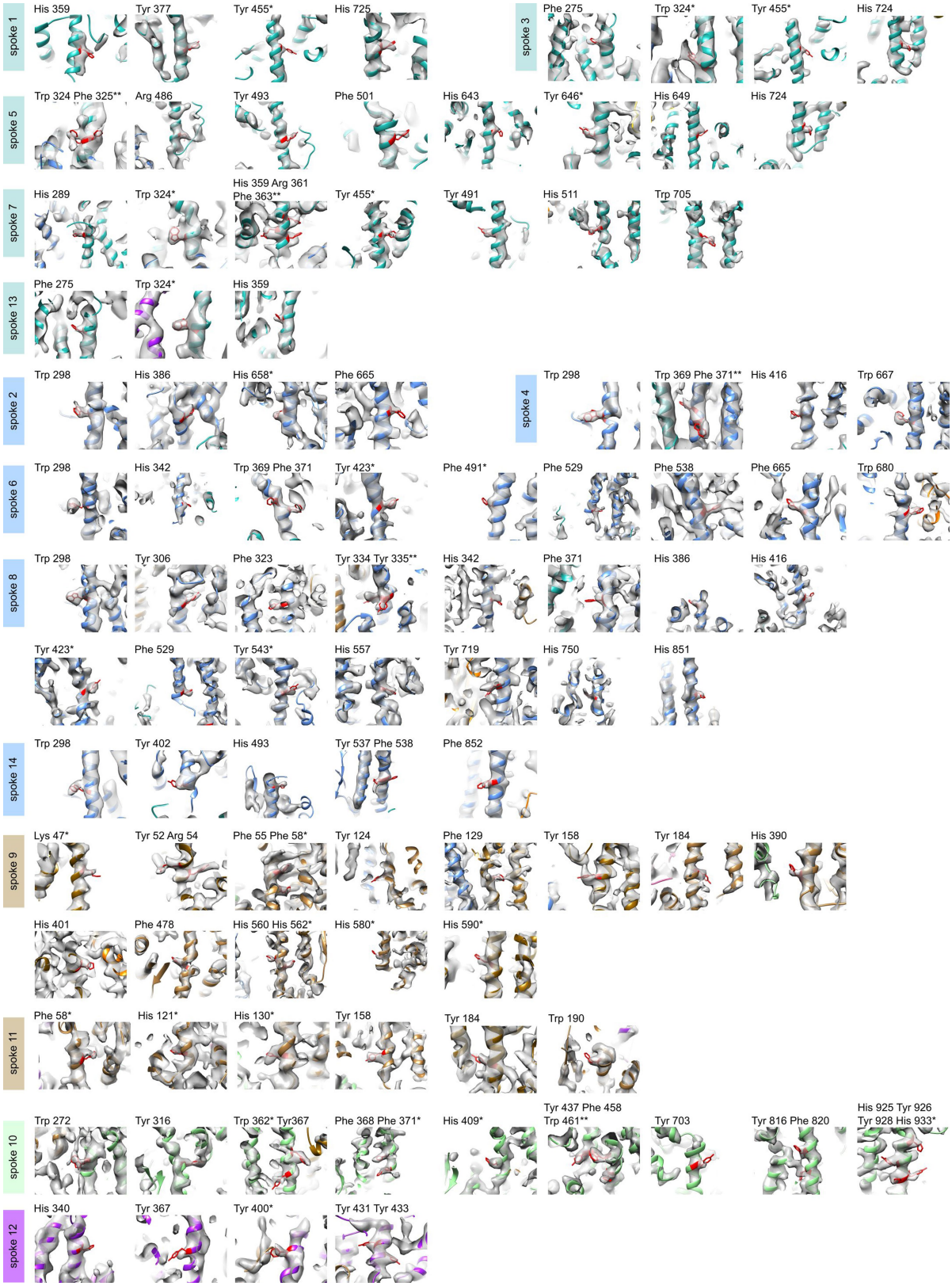

Extended Data Fig. 5 | Gallery of bulky amino acid side chains resolved in the γ-TuRC density. GCP-variant-specific bulky amino acid side chains are marked by an asterisk. Combinations of such side chains in close proximity are marked by two asterisks.

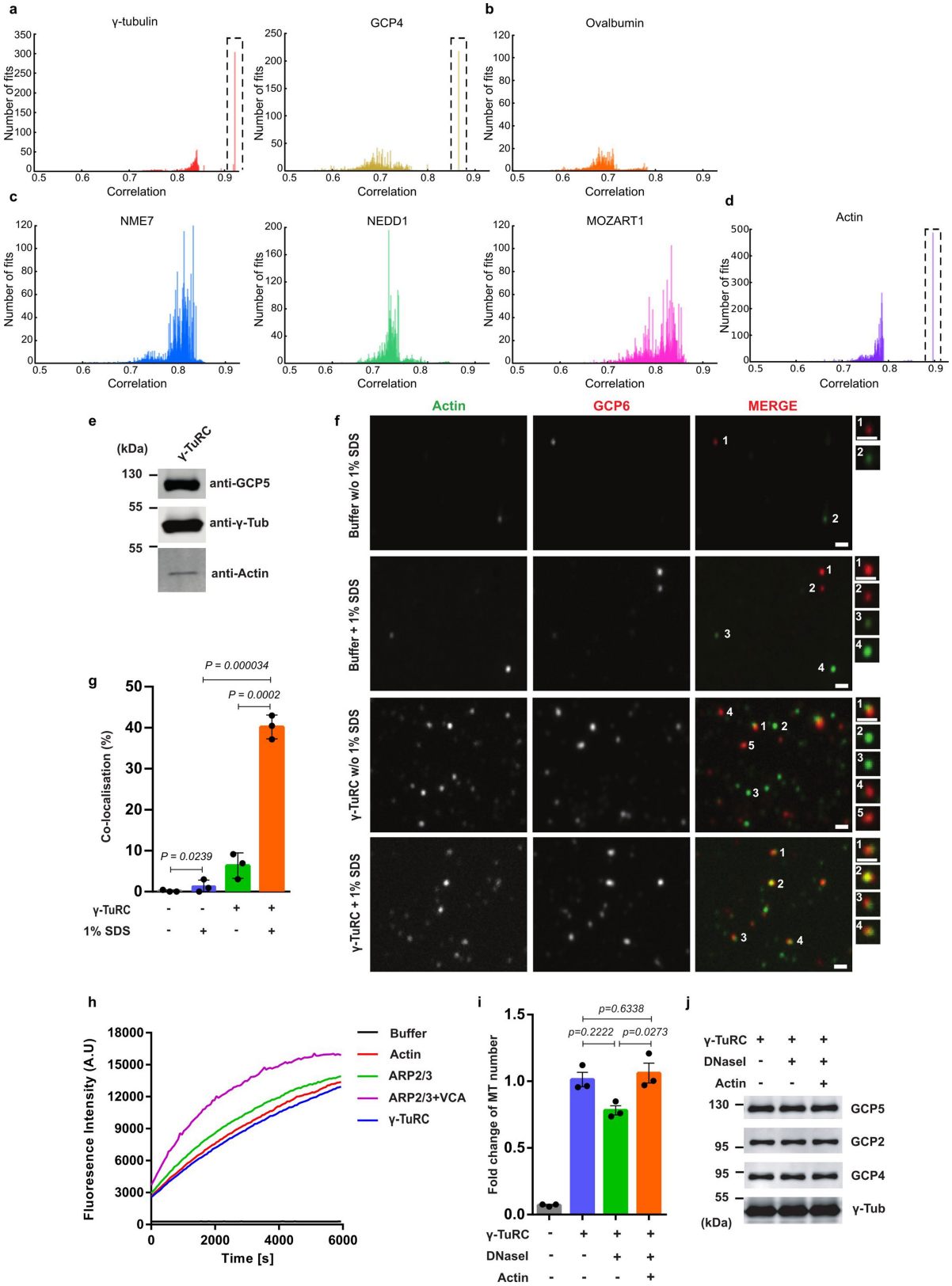

Extended Data Fig. 6 | See next page for caption.

Extended Data Fig. 6 | Actin is a bona fide γ-TuRC component involved in MT nucleation. a–**d**, High-confidence homology models were docked with 10,000 randomly sampled starting positions and orientations into the envelope of the cryo-EM density. The number of fits is plotted against the respective correlation coefficients. **a**, γ-Tubulin and GCP4 served as positive controls. True positive fits correspond to redundant high-frequency fits with high correlation coefficients (dashed box). **b**, Ovalbumin served as negative control. No redundant high-frequency fits with high correlation coefficient indicative of a true positive match were observed. **c**, Unbiased fitting of NME7, NEDD1 and MOZART1 resulted in a distribution of correlation coefficients similar to the negative control, indicating no positive fit. **d**, Unbiased fitting of actin resulted in a distribution of correlation coefficients similar to the positive controls, clearly including a true positive fit (dashed box) shown in Fig. 1a. **e**, Purified γ-TuRCs from *X. laevis* egg extracts were resolved by SDS–PAGE and immunoblotted with anti-γ-tubulin, anti-GCP5 and anti-actin antibodies, which confirms that actin is associated with the purified γ-TuRC fraction. Representative blots are from three biologically independent experiments. For gel source data, see Supplementary Fig. 1. **f**, **g**, Indirect immunofluorescence of adsorbed γ-TuRC rings with antibodies directed against actin and GCP6 indicates colocalization of both proteins. Treatment with 1% SDS increased the antibody accessibility of actin located in the spatially confined interior of the γ-TuRC. **f**, Representative fluorescence images together with magnified views from three biologically independent experiments. Scale bars, 20 nm. **g**, Percentage of colocalization events of actin and GCP6 normalized to the GCP6 signal. After treatment with 1% SDS, 40.2% of GCP6 signals colocalized with actin signals. In the absence of 1% SDS, colocalization events decreased to 6.4% owing to inaccessibility of the epitope. Data are mean ± s.d. from $n = 3$ biologically independent experiments. P values were determined by unpaired two-sided t-test. **h**, Actin polymerization activity was tested for buffer with and without pyrene F-actin and 0.5 nM ARP2/3, 0.5 nM ARP2/3 with 15 nM VCA and 0.5 nM γ-TuRC with pyrene F-actin. The purified γ-TuRC is devoid of actin nucleation activity. The fluorescence intensity change was determined over time. Data are the mean of five independent experiments. **i**, γ-TuRC MT nucleation activity after pre-incubation with buffer, the actin-binding protein DNaseI and the preformed actin–DNaseI complex. $n = 3$ biologically independent experiments; data are mean ± s.e.m. P values were determined by unpaired two-sided t-test. **j**, After 3 h incubation on ice, before the MT nucleation assay, samples were analysed by immunoblotting to confirm that equal amounts γ-TuRC were present in different experimental groups. Three biologically independent experiments were performed with similar results. For gel source data, see Supplementary Fig. 1.

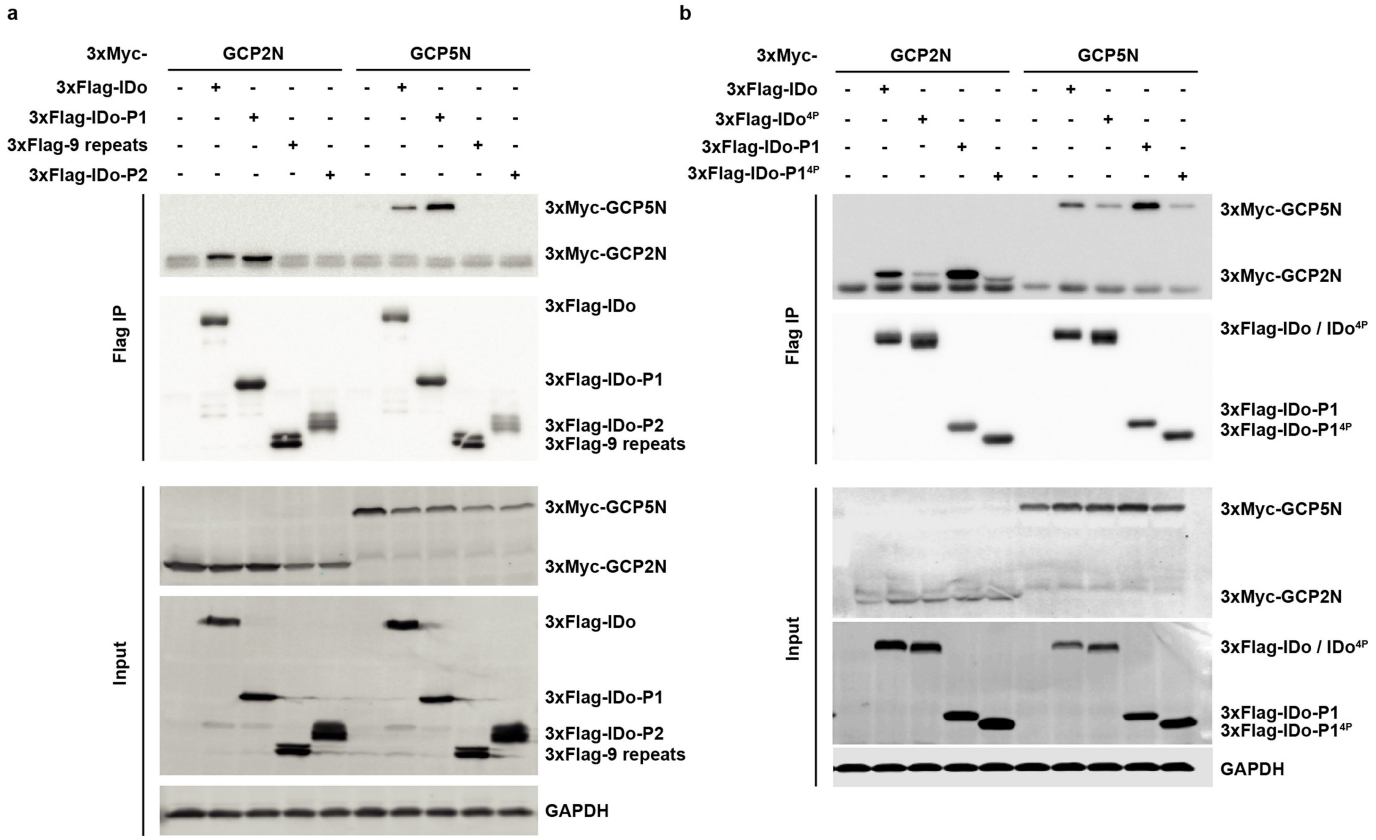

Extended Data Fig. 7 | Co-immunoprecipitation of wild-type or mutant 3×Flag–GCP6 insertion domain fragments with the 3×Myc-tagged GCP2 and GCP5 N termini. a, Co-immunoprecipitation of the GCP6 insertion domain (IDo; residues 606–1499), part 1 of the GCP6 insertion domain (IDo-P1; residues 606–1026), GCP6 insertion domain 9 repeats (IDo-9 repeats; residues 1027–1268) and part 2 of the GCP6 insertion domain (IDo-P2; residues 1269–1499) (as defined in Fig. 3a) with GCP2-N and GCP5-N. Immunoblotting was performed with indicated antibodies. Representative result is from three independent experiments. For gel source data, see Supplementary Fig. 1. **b**, Co-immunoprecipitation of the GCP6 insertion domain or part 1 of the GCP insertion domain with residues V644, F706, F732 and Q783 mutated to proline (GCP6-IDo^{4P} and GCP6-IDo-P1^{4P}, respectively) with both GCP2-N and GCP5-N. Immunoblotting was performed with indicated antibodies. Three biologically independent experiments were performed with similar results. For gel source data, see Supplementary Fig. 1.

Extended Data Fig. 8 | Sequence conservation of the GCP6 insertion domain region. The GCP6 insertion domains from human, bovine, mouse, chicken, *X. laevis*, *Anolis carolinensis* and medaka (*Oryzias latipes*) were aligned with Clustal Omega (default settings) build in Jalview software[42–44]. The mutations in the 4P mutant (V644P, F706P, F732P and Q783P) are indicated by asterisks. The individual repeats of the nine-repeat structure in human GCP6 are marked by arrows.

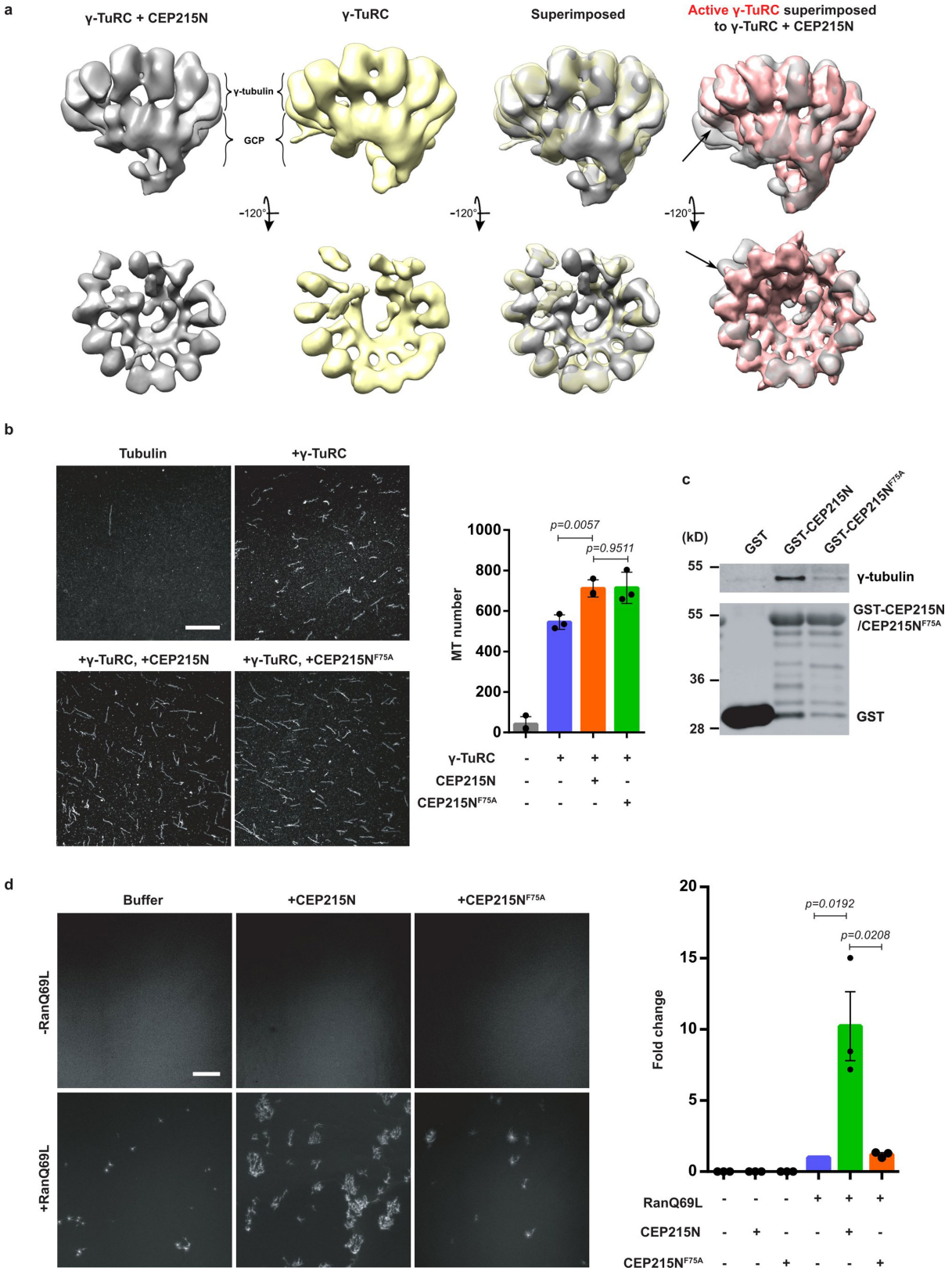

Extended Data Fig. 9 | See next page for caption.

Extended Data Fig. 9 | The CM1 motif of CEP215-N is not sufficient to activate the MT nucleation activity of γ-TuRC. a, γ-TuRC particles with or without a 600-fold excess of CEP215-N were analysed by negative-staining electron microscopy. The resulting 3D densities (grey, yellow) were superimposed and compared to a simulated density of the γ-TuRC in the extrapolated active conformation (red). Arrows indicate the most pronounced structural differences (transparent grey density not filled by red density) between the CEP215-N–γ-TuRC complex and the simulated density of the γ-TuRC in the extrapolated active conformation. **b**, γ-TuRC (0.5 nM) was incubated with an excess of CEP215-N or CEP215(F75A)-N (3 μM). In vitro MT nucleation activity of the γ-TuRC incubated with buffer, glutathione *S*-transferase (GST), GST–CEP215-N or GST–CEP215(F75A)-N. $n = 3$ biologically independent experiments; data are mean ± s.d. *P* values were determined by unpaired two-sided *t*-test. Scale bar, 10 μm. **c**, In vitro binding of γ-TuRC to purified and recombinant GST, CEP215-N and CEP215(F75A)-N. Immunoblots were probed with anti-γ-tubulin and anti-GST antibodies as shown. Three biologically independent experiments were performed with similar results. For gel source data, see Supplementary Fig. 1. **d**, MT nucleation activity in egg extracts induced by the addition of Ran(Q69L) and CEP215-N. The MT nucleation reaction was stopped after 15 min at 20 °C when Ran(Q69L) addition only induced a small number of MTs. Fold changes of total aster fluorescence intensity from ten random fields were quantified and normalized to the group adding Ran(Q69L) and without CEP215-N or CEP215(F75A)-N. $n = 3$ biologically independent experiments; data are mean ± s.e.m. *P* values were determined by unpaired two-sided *t*-test. Scale bars, 50 μm.

Extended Data Table 1 | Cryo-EM data collection, refinement and validation statistics

	#1 γ-TuRC (EMDB-10491) (PDB 6TF9)			
Data collection and processing	**dataset 1**	**dataset 2**	**dataset 3**	**dataset 4**
Magnification	42,000	42,000	42,000	64,000
Voltage (kV)	300	300	300	300
Electron exposure (e–/Å^2)	35	42	51	57.4
Defocus range (μm)	-1.5 to -3.5	-1.5 to -3.5	-1.5 to -3.5	-1.0 to -3.0
Pixel size (Å)	2.1	2.1	2.1	1.35
Symmetry imposed	C1	C1	C1	C1
Initial particle images (no.)	774255	1174825	908652	2624596
Final particle images (no.)	17633	5621	7962	14880
Merged set of particles	46096			
Map resolution (Å)	4.8			
FSC threshold	0.143			
Map resolution range (Å)	4.5-6.0			
Refinement				
Initial model used (PDB code)	Homology models derived from GCP4 (3RIP), γ-tubulin (1Z5W) and Actin (1J6Z)			
Model resolution (Å)	4.75			
FSC threshold	0.143			
Model resolution range (Å)	4.75-6.89			
Map sharpening *B* factor (Å^2)	-180.0			
Model composition				
Non-hydrogen atoms	120125			
Protein residues	14974			
Ligands	0			
B factors (Å^2)				
Protein	141.25			
Ligand	--			
R.m.s. deviations				
Bond lengths (Å)	0.005			
Bond angles (°)	1.051			
Validation				
MolProbity score	1.99			
Clashscore	4.90			
Poor rotamers (%)	2.73			
Ramachandran plot				
Favored (%)	93.91			
Allowed (%)	5.85			
Disallowed (%)	0.24			

nature research

Corresponding author(s): Elmar Schiebel, Stefan Pfeffer

Last updated by author(s): Dec 4, 2019

Reporting Summary

Nature Research wishes to improve the reproducibility of the work that we publish. This form provides structure for consistency and transparency in reporting. For further information on Nature Research policies, see Authors & Referees and the Editorial Policy Checklist .

Statistics

For all statistical analyses, confirm that the following items are present in the figure legend, table legend, main text, or Methods section.

n/a	Confirmed	
☐	☒	The exact sample size (*n*) for each experimental group/condition, given as a discrete number and unit of measurement
☐	☒	A statement on whether measurements were taken from distinct samples or whether the same sample was measured repeatedly
☐	☒	The statistical test(s) used AND whether they are one- or two-sided *Only common tests should be described solely by name; describe more complex techniques in the Methods section.*
☐	☒	A description of all covariates tested
☐	☒	A description of any assumptions or corrections, such as tests of normality and adjustment for multiple comparisons
☐	☒	A full description of the statistical parameters including central tendency (e.g. means) or other basic estimates (e.g. regression coefficient) AND variation (e.g. standard deviation) or associated estimates of uncertainty (e.g. confidence intervals)
☐	☒	For null hypothesis testing, the test statistic (e.g. *F*, *t*, *r*) with confidence intervals, effect sizes, degrees of freedom and *P* value noted *Give P values as exact values whenever suitable.*
☒	☐	For Bayesian analysis, information on the choice of priors and Markov chain Monte Carlo settings
☒	☐	For hierarchical and complex designs, identification of the appropriate level for tests and full reporting of outcomes
☒	☐	Estimates of effect sizes (e.g. Cohen's *d*, Pearson's *r*), indicating how they were calculated

Our web collection on statistics for biologists contains articles on many of the points above.

Software and code

Policy information about availability of computer code

Data collection	Datasets for cryo-EM were collected with SerialEM (3.7). Data for CD analysis were collected using JASCO spectra manager (1.06.00). Data for immunoblots were collected either by LAS4000IR (2.1) or Image Studio (5.2). Datasets for negative stain EM were collected with SerialEM (1.0.0.1). Software WoRx (6.1.1) was used to collect the data for immunofluorescence experiment. Data for in vitro nucleation assay and egg extract experiment were collected by VisiView software. Data for Actin polymerization assay were collected by CLARIOstar.
Data analysis	EM data were processed using Relion 3.0-Beta, MotionCorr 2.0 and gCTF 1.06. All density map related figure were prepared in Chimera 1.13.1 and ChimeraX 0.9. Atomic modelling was done in Coot 0.8.9.2 and Coot 0.9. Molecular Flexible fitting was performed in QwikMD implemented in VMD 1.9.4.a35 and in NAMD 2.13. Refinement and final flexible fitting of the model was performed in website tool NAMDinator, and in Phenix 1.14. Data for γ-TuRC geometrical analysis of tubulins and for CD analysis were plotted in Gnuplot 5.2. Secondary structure predictions were done in website tool PSIPRED vs 3.0. Sequence alignment of GCP components was done in website tool PROMALS-3D. Analysis and vector visualisation of conformational change of γ-TuRC was performed in PyMol 2.2.3. Data for CD measurements were analyzed using JASCO spectra manager (1.06.00). MaxQuant software (1.6.2.6a) was used for LC-MS/MS analysis and database search. Fiji software (2.0.0-rc-46/1.50g) was used to to analyze the microtubule nucleation and immunofluorescence data, and western blots images. Microsoft Office Excel (2011) was used to normalize the data before statistical analyses. GraphPad Prism 6 (6.01) was used for statistical analyses. Image Studio Lite (5.2.5) was used for western blot quantification in salt treatments. EMAN2 Project Manager (eman2.12) was used for negative stain EM particle picking, an the particles were classified and averaged using the IMAGIC-4D package. The GCP6 IDo domain alignment was performed with Clustal Omega build in Jalview software (2101-VM).

For manuscripts utilizing custom algorithms or software that are central to the research but not yet described in published literature, software must be made available to editors/reviewers. We strongly encourage code deposition in a community repository (e.g. GitHub). See the Nature Research guidelines for submitting code & software for further information.

Data

Policy information about availability of data

All manuscripts must include a data availability statement. This statement should provide the following information, where applicable:

- Accession codes, unique identifiers, or web links for publicly available datasets
- A list of figures that have associated raw data
- A description of any restrictions on data availability

Cryo-EM densities of the γ-TuRC filtered according to global or local resolution were deposited in the Electron Microscopy Data Bank (EMDB) under accession code EMD-10491. Atomic coordinates for the γ-TuRC were deposited at the Protein Data Bank (PDB) under accession code 6TF9. The original immunoblots and further source data from LFQ mass spectrometry (Fig. 2a), immunoblot quantification (Fig. 3c), geometric analysis of the atomic model (Figs. 3g, 4b, 4c, 4d), MT nucleation assays (Extended Data Figs. 1c, 6i, 9b, 9d), CD measurements (Extended Data Fig. 4e), unbiased structure-guided identification (Extended Data Fig. 6a-d), quantification of indirect immunofluorescence (Extended Data Fig. 6g) and Actin polymerization (Extended Data Fig. 6h) are included in the Supplementary Information. The raw cryo-EM micrograph movie stacks are available from the corresponding authors upon request.

Field-specific reporting

Please select the one below that is the best fit for your research. If you are not sure, read the appropriate sections before making your selection.

☒ Life sciences ☐ Behavioural & social sciences ☐ Ecological, evolutionary & environmental sciences

For a reference copy of the document with all sections, see nature.com/documents/nr-reporting-summary-flat.pdf

Life sciences study design

All studies must disclose on these points even when the disclosure is negative.

Sample size	No statistical methods were used to predetermine sample size. Cryo-EM data were collected in a sufficient amount for reconstruction. For immunofluorescence and microtubule in vitro nucleation experiments, images were acquired in a number that is sufficient for statistic analysis (as specified in Methods). For negative stain EM, the images used for particle classification and average were enough to get clear views of the protein complexes. Sample size was chosen based on data variation.
Data exclusions	No data were excluded from the analyses.
Replication	All experiments, including the immunoprecipitation, mass spectrometry, and so on, were repeated at least three times to confirm the reproducibility. All replicates were successful.
Randomization	For immunofluorescence, mass spec analysis and microtubule in vitro nucleation experiments, images/data were acquired randomly. Other experiments were not related to randomization.
Blinding	Blinding was not applied to our study. For a number of experiments this was technically not possible: cyro-EM, IP experiment, CD measurments. For other experiments this was technically not feasible because of the large sample size: e.g. MT nucleation assays. In other cases, a finding was confirmed by an independent approach: e.g. actin in the γ-TuRC.

Reporting for specific materials, systems and methods

We require information from authors about some types of materials, experimental systems and methods used in many studies. Here, indicate whether each material, system or method listed is relevant to your study. If you are not sure if a list item applies to your research, read the appropriate section before selecting a response.

Materials & experimental systems

n/a	Involved in the study
☐	☒ Antibodies
☐	☒ Eukaryotic cell lines
☒	☐ Palaeontology
☐	☒ Animals and other organisms
☒	☐ Human research participants
☒	☐ Clinical data

Methods

n/a	Involved in the study
☒	☐ ChIP-seq
☒	☐ Flow cytometry
☒	☐ MRI-based neuroimaging

Antibodies

Antibodies used	Anti-γ-tubulin rabbit polyclonal antibody, which was used for γ-TuRC purification, was homemade against the C-terminal peptide as described in the previous publication: doi: 10.1038/ncomms9722, and diluted 1:2000 in immunoblot in CEP215N pull-down assay. Anti-γ-tubulin mouse monoclonal antibody (GTU-88, T6557, Lot: 053K4839), which was used for immunoblotting, was

from Sigma-Aldrich and was diluted 1:4000. Rabbit anti-GCP2 polyclonal antibody (PA5-21433, Lot: QL2122721A) was from Thermo Fisher Scientific, and was diluted 1:1000 for immunoblotting. Rabbit anti-Xgrip109 (GCP3) polyclonal antibody, diluted 1:2000 in immunoblotting, was from Dr. Y. Zheng, and was previously described in the publication: DOI: 10.1083/jcb.141.3.675. Rabbit anti-GCP6 polyclonal antibody, diluted 1:2000 in immunoblotting, was from Dr. Y. Zheng, and was described in the previous publication: DOI: 10.1083/jcb.151.7.1525. Guinea pig anti-GCP6 polyclonal antibody for immunofluorescence was generated as described in in the previous publication: DOI: 10.1083/jcb.151.7.1525, and was diluted 1:200. Anti-β-Actin mouse monoclonal antibody (AC-74, A5316, Lot: 048M4843V) used in immunofluorescence (diluted 1:1000) and anti-Actin rabbit polyclonal antibody (A2066, Lot: 058M4812V) used in immunoblot (diluted 1:200) were from Sigma-Aldrich. Anti-GCP4 rabbit polyclonal antibody were raised against full-length purified GCP4, and was diluted 1:200 in immunoblotting. Anti-GCP5 mouse monoclonal antibody (E-1) was from Santa Cruz Biotechnology (sc-365837, Lot: E2014), and was diluted 1:500 in immunoblotting. Mouse anti-FLAG monoclonal antibody (9A3, 8146S, Lot: 3, diluted 1:500 in immunoblotting) and rabbit anti-GAPDH polyclonal antibody (14C10, 2118S, Lot: 10, diluted 1:1000 in immunoblotting) were from Cell Signaling Technology. Mouse monoclonal anti-c-Myc antibody (clone 9E10, M4439, Lot: 087M4765V, diluted 1:1000 in immunoblotting) was from Sigma-Aldrich. Secondary antibodies used in this study were: Donkey anti-Mouse Alexa Fluor 488-conjugated antibody (A21202, Lot: 1562298, diluted 1:500 in immunofluorescence) and goat anti-guinea pig Alexa Fluor® 555-conjugated antibody (A21435, Lot: 1711692, diluted 1:500 in immunofluorescence) are from Thermo Fisher Scientific; peroxidase-conjugated goat anti-mouse antibody (115-035-068, Jackson ImmunoResearch Laboratories, diluted 1:5000 in immunoblotting); donkey anti-mouse DyLight 680 (A10038, Lot: 1717043) and 800-conjugated antibodies (SA5-10172) are from Thermo Fisher Scientific, and both were diluted 1:5000 in immunoblotting; anti-rabbit DyLight 680-conjugated antibody (5366S, Lot: 3, Cell Signaling Technology, diluted 1:5000 in immunoblotting); IRDye 800CW Donkey anti-Rabbit IgG (926-32213, Lot: C61012-02, LI-COR Biosciences, diluted 1:5000 in immunoblotting).

Validation

Homemade rabbit anti-γ-tubulin rabbit polyclonal antibody and homemade rabbit anti-GCP4 rabbit polyclonal antibodies were validated previously in the publication: doi: 10.1038/ncomms9722

Homemade rabbit anti-GCP3 rabbit polyclonal antibody was validated previously in the publication: DOI: 10.1083/jcb.141.3.675

Homemade rabbit anti-GCP6 rabbit polyclonal antibody was validated previously in the publication: DOI: 10.1083/jcb.151.7.1525

Homemade Guinea pig anti-GCP6 polyclonal antibody was generated with the same epitope as homemade rabbit anti-GCP6 rabbit polyclonal antibody (DOI: 10.1083/jcb.151.7.1525), and was further validated by pilot experiments before using.

All commercial antibodies were validated by manufacturers for the species and applications, which can be found in the links below.

Anti-γ-tubulin mouse monoclonal antibody (GTU-88):

https://www.sigmaaldrich.com/catalog/product/sigma/t6557?lang=de&region=DE

Rabbit anti-GCP2 polyclonal antibody: https://www.thermofisher.com/antibody/product/GCP2-Antibody-Polyclonal/PA5-21433

Anti-β-Actin mouse monoclonal antibody (AC-74):

https://www.sigmaaldrich.com/catalog/product/sigma/a2228?lang=de&region=DE

Anti-Actin rabbit polyclonal antibody (A2066):

https://www.sigmaaldrich.com/catalog/product/sigma/a2066?lang=de&region=DE

Anti-GCP5 mouse monoclonal antibody (E-1): https://www.scbt.com/scbt/product/gcp5-antibody-e-1

Mouse anti-FLAG monoclonal antibody (9A3):

https://en.cellsignal.de/products/primary-antibodies/dykddddk-tag-9a3-mouse-mab-binds-to-same-epitope-as-sigma-s-anti-flag-m2-antibody/8146

Rabbit anti-GAPDH polyclonal antibody (14C10):

https://en.cellsignal.de/products/primary-antibodies/gapdh-14c10-rabbit-mab/2118

Mouse monoclonal anti-c-Myc antibody (clone 9E10):

https://www.sigmaaldrich.com/catalog/product/sigma/m4439?lang=de&region=DE&gclid=CjwKCAjwkqPrBRA3EiwAKdtwk-gHHmK21m-8cwvWs0O4fsjAXJMo3waZRhaAnZ8eq5IsEdpYzebNXBoC_qQQAvD_BwE

Donkey anti-Mouse Alexa Fluor 488-conjugated antibody: https://www.thermofisher.com/antibody/product/Donkey-anti-Mouse-IgG-H-L-Highly-Cross-Adsorbed-Secondary-Antibody-Polyclonal/A-21202

Goat anti-guinea pig Alexa Fluor® 555-conjugated antibody: https://www.thermofisher.com/antibody/product/Goat-anti-Guinea-Pig-IgG-H-L-Highly-Cross-Adsorbed-Secondary-Antibody-Polyclonal/A-21435

Peroxidase-conjugated goat anti-mouse antibody: https://www.jacksonimmuno.com/catalog/products/115-035-068

Donkey anti-mouse DyLight 680-conjugated antibody: https://www.thermofisher.com/antibody/product/Donkey-anti-Mouse-IgG-H-L-Highly-Cross-Adsorbed-Secondary-Antibody-Polyclonal/A10038

Donkey anti-mouse DyLight 800-conjugated antibody: https://www.thermofisher.com/antibody/product/Donkey-anti-Mouse-IgG-H-L-Cross-Adsorbed-Secondary-Antibody-Polyclonal/SA5-10172

Anti-rabbit DyLight 680-conjugated antibody: https://en.cellsignal.de/products/secondary-antibodies/anti-rabbit-igg-h-l-dylight-680-conjugate/5366

IRDye 800CW Donkey anti-Rabbit IgG: https://www.licor.com/bio/reagents/irdye-800cw-donkey-anti-rabbit-igg-secondary-antibody

Eukaryotic cell lines

Policy information about cell lines

Cell line source(s)	HEK293T cell line is as described (Panic, M, et. al. PLOS Genet. 11, e1005243 (2015).
Authentication	We verified the HEK293T cell line according to the morphology by light microscopy. Cell line was purchased from ATCC.
Mycoplasma contamination	HEK293T cell line was negative in the mycoplasma contamination test.

Commonly misidentified lines (See ICLAC register)	No commonly misidentified lines were used in this study.

Animals and other organisms

Policy information about studies involving animals; ARRIVE guidelines recommended for reporting animal research

Laboratory animals	Xenopus laevis (lab bread NASCO, USA), female, sexually mature, i.e. more than 9 months old.
Wild animals	No wild animals were used in this study.
Field-collected samples	No field-collected samples were used in this study.
Ethics oversight	The permission numbers for Xenopus laevis experiment are:35-9185.81/G-204/12 (Regierungspräsidium Karlsruhe, BW) ; 81-02.05.40.17.091 (LANUF Recklinghausen, NRW). Ethic justification of experiment is according to § 7a Abs. 2 Nr. 3 TierSchG.

Note that full information on the approval of the study protocol must also be provided in the manuscript.